

PAPER

Method for Estimating Scatterer Information from the Response Waveform of a Backward Transient Scattering Field Using TD-SPT

Keiji GOTO^{†a)}, Toru KAWANO[†], *Members*, Munetoshi IWAKIRI[†], Tsubasa KAWAKAMI[†],
and Kazuki NAKAZAWA[†], *Nonmembers*

SUMMARY This paper proposes a scatterer information estimation method using numerical data for the response waveform of a backward transient scattering field for both E- and H-polarizations when a two-dimensional (2-D) coated metal cylinder is selected as a scatterer. It is assumed that a line source and an observation point are placed at different locations. The four types of scatterer information covered in this paper are the relative permittivity of a surrounding medium, the relative permittivity of a coating medium layer and its thickness, and the radius of a coated metal cylinder. Specifically, a time-domain saddle-point technique (TD-SPT) is used to derive scatterer information estimation formulae from the amplitude intensity ratios (AIRs) of adjacent backward transient scattering field components. The estimates are obtained by substituting the numerical data of the response waveforms of the backward transient scattering field components into the estimation formulae and performing iterative calculations. Furthermore, a minimum thickness of a coating medium layer for which the estimation method is valid is derived, and two kinds of applicable conditions for the estimation method are proposed. The effectiveness of the scatterer information estimation method is verified by comparing the estimates with the set values. The noise tolerance and convergence characteristics of the estimation method and the method of controlling the estimation accuracy are also discussed.

key words: scatterer information estimation method, response waveform, backward transient scattering field, time-domain saddle-point technique (TD-SPT), amplitude intensity ratios (AIRs)

1. Introduction

Since the publication of Keller's paper until today, a number of researchers have presented various research results on the problem of electromagnetic scattering by two-dimensional (2-D) cylindrical objects [1]–[19]. The 2-D cylindrical objects are classified as metallic cylinders [1]–[4], [6], [8], [9], [14], dielectric cylinders [10], [13], [15], and coated metal cylinders [5], [7], [10]–[12], [16]–[19]. Typical examples of applications include the estimation of radar cross sections (RCSs) of objects such as aircraft [2]–[11], [14], [15] and the non-destructive deterioration diagnosis of reinforced concrete [17]–[19].

When an object is illuminated with a pulse wave, transient scattering waves are reemitted from the object. A response waveform of a transient scattering field contains scatterer information such as the structure, dimensions, and material of a scatterer. Research results on transient scatter-

ing fields from 2-D coated metal cylinders [12], [17]–[19] have made it possible to calculate response waveforms with high accuracy. However, these research results are difficult to analytically extract the transient scattering field components with different propagation paths that constitute the response waveforms.

The authors have derived high-frequency (HF) asymptotic solutions for a transient scattering field from a coated metal cylinder, namely a time-domain asymptotic-numerical solution (TD-ANS) [20]–[22], a TD saddle-point technique (TD-SPT) [23], [24], and a TD Fourier transform method (TD-FTM) [25], [26]. The HF asymptotic solutions for a backward transient scattering field [22]–[26] are represented by a superposition of a direct geometric optical ray (DGO) and a reflected GO (RGO) series. As a *first step* to estimate the scatterer information, we considered an interpretation method for the inversion phenomena of the response waveforms [23]. As a *second step*, we investigated an interpretation method for the amplitude intensities of the response waveforms [26].

The purpose of this paper is to propose a scatterer information estimation method using numerical data for the response waveform of a backward transient scattering field for both E- and H-polarizations when a 2-D coated metal cylinder is selected as a scatterer [27]. A line source and an observation point are assumed to be placed at different locations. The four types of scatterer information covered in this paper are the relative permittivity of a surrounding medium, the relative permittivity of a coating medium layer and its thickness, and the radius of a coated metal cylinder.

Specifically, scatterer information estimation formulae are to be derived from the amplitude intensity ratios (AIRs) of adjacent backward transient scattering field components using the TD-SPT [23]. The numerical data of the response waveforms of the backward transient scattering field components will be substituted into the estimation formulae and iterative calculations will be performed to obtain estimates. In addition, we will derive a minimum thickness of a coating medium layer for which the estimation method is valid, and propose two kinds of applicable conditions for the estimation method. The effectiveness of the scatterer information estimation method will be verified by comparing the estimates with the set values. The noise tolerance and convergence characteristics of the estimation method and the method of controlling the estimation accuracy will be also discussed.

The time dependence $\exp(-i\omega t)$ is assumed but sup-

Manuscript received September 3, 2023.

Manuscript revised December 12, 2023.

Manuscript publicized January 23, 2024.

[†]The National Defense Academy of Japan, Yokosuka-shi, 239–8686 Japan.

a) E-mail: keigoto@nda.ac.jp

DOI: 10.1587/transle.2023ECP5040

pressed throughout the text.

2. Formulation

Figure 1 shows a cross-sectional geometry of a 2-D coated metal cylinder of radius $\rho = a (= b + h)$, which is made of a metal cylinder of radius $\rho = b$ coated with a coating medium 2 (ε_2, μ_0) of thickness $h (= a - b)$, and coordinate systems (x, y, z) and (ρ, ϕ) . The symbol ε_2 is a permittivity defined by $\varepsilon_2 = \varepsilon_0 \varepsilon_{2r}$ where ε_{2r} is a relative permittivity. The constitutive parameters ε_0 and μ_0 are a permittivity and a permeability in free space, respectively. An electric or magnetic line source $Q(\rho_0, \phi_0)$ is placed parallel to the central axis of the coated metal cylinder in a surrounding medium 1 (ε_1, μ_0), where ε_1 is defined by $\varepsilon_1 = \varepsilon_0 \varepsilon_{1r}$ and ε_{1r} is a relative permittivity. An observation point $P(\rho \neq \rho_0, \phi = \phi_0)$ in the medium 1 is placed at a different location from the line source Q . The permittivity of medium 1 and that of medium 2 are both assumed to be lossless and $\varepsilon_1 < \varepsilon_2$. The thickness h of the coating medium 2 is assumed to be greater than or equal to a minimum thickness h_c , namely $h \geq h_c$ (see (26) and (27)), which satisfies the applicable condition of the estimation method (see Sect. 4.4).

Figure 2 shows the propagation paths of the DGO and RGO components (\rightarrow : solid curve with arrow) when a cylindrical pulse wave emitted from the line source Q is incident perpendicularly on a coated metal cylinder.

3. AIRs Using the TD-SPT

3.1 UWB Pulse Source

We assume a truncated Gaussian-type modulated pulse source $s(t)$ placed at the point Q [20]–[23], [27]

$$s(t) = \begin{cases} \exp \left[-i\omega_0(t - t_0) - \frac{(t - t_0)^2}{(2d)^2} \right] & \text{for } 0 \leq t \leq 2t_0 \\ 0 & \text{elsewhere} \end{cases} \quad (1)$$

where ω_0 is a central angular frequency, and t_0 and d are constant parameters. The frequency spectrum $S(\omega)$ of $s(t)$ is given by the following equation using the error function $\text{erf } z$ [28].

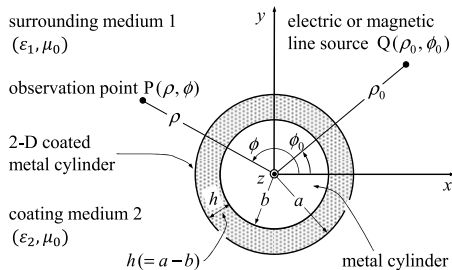


Fig. 1 2-D coated metal cylinder, and coordinate systems (x, y, z) and (ρ, ϕ) . $Q(\rho_0, \phi_0)$: electric or magnetic line source, $P(\rho, \phi)$: observation point.

$$S(\omega) = 2d\sqrt{\pi} \text{Re}[\text{erf } \beta(\omega)] \exp\{i\omega t_0 - d^2(\omega - \omega_0)^2\} \quad (2)$$

$$\beta(\omega) = \frac{t_0}{2d} - id(\omega - \omega_0) \quad (3)$$

$$\text{erf } z = \frac{2}{\sqrt{\pi}} \int_0^z \exp(-t^2) dt. \quad (4)$$

Figures 3 (a) and 3 (b) show the real part of $s(t)$ and the absolute value of $S(\omega)$, respectively. The numerical parameters used in the calculations are given in the caption of Fig. 3. For these numerical parameters, the fractional bandwidth (FB) of $S(\omega)$ is 0.34, which satisfies the ultra-wideband (UWB) definition (FB > 0.25) [29]. Therefore, $s(t)$ in Fig. 3 is a UWB pulse source.

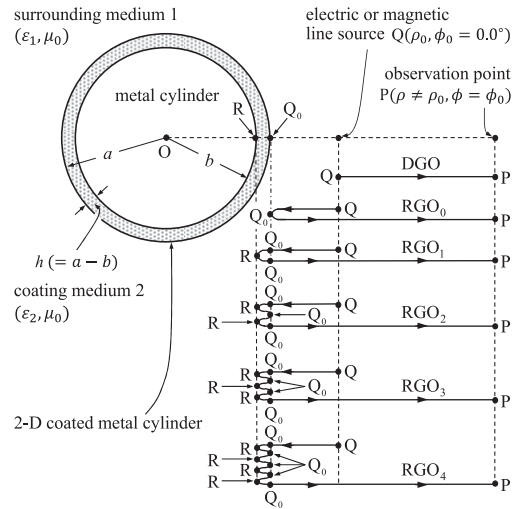


Fig. 2 Schematic diagram of backward transient scattering from a 2-D coated metal cylinder. Location of the electric or magnetic line source $Q(\rho_0, \phi_0 = 0.0^\circ)$ and that of the observation point $P(\rho \neq \rho_0, \phi = \phi_0)$. The propagation paths of backward transient scattering field components: DGO($Q \rightarrow P$), $\text{RGO}_{p=0} = \text{RGO}_0(Q \rightarrow Q_0 \rightarrow P)$, $\text{RGO}_{p=1} = \text{RGO}_1(Q \rightarrow Q_0 \rightarrow R \rightarrow Q_0 \rightarrow P)$, and $\text{RGO}_p(Q \rightarrow p(Q_0 \rightarrow R \rightarrow)Q_0 \rightarrow P)$. The propagation path $p(Q_0 \rightarrow R \rightarrow)Q_0$ indicates multiple reflection effect in a coating medium 2. The p denotes the number of reflections at the point R on a metal surface of radius $\rho = b$.

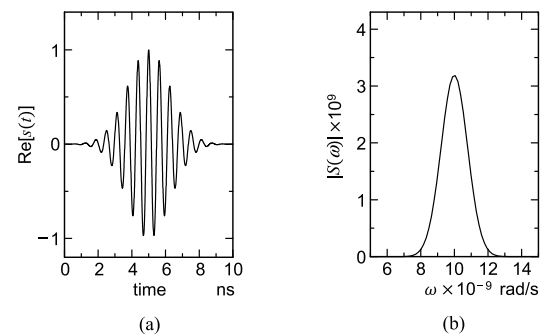


Fig. 3 Truncated Gaussian-type modulated UWB pulse source $s(t)$ defined by (1). (a) Real part of $s(t)$. (b) Absolute value of $S(\omega)$. Numerical parameters: $\omega_0 = 1.0 \times 10^{10}$ rad/s, $t_0 = 5.0 \times 10^{-9}$ s, $d = 9.0 \times 10^{-10}$ s, and FB = 0.34.

3.2 Derivation of the AIRs Using the TD-SPT

The backward transient scattering field component in (A·2) shown in Appendix, which constitutes the TD-SPT in (A·1), takes a peak and its arrival time of the response waveform $\text{Re}[y_{j,\text{SPT},\ell}(t)]$, $j = \text{E, H}$ as follows [27]

$$\text{Re}[y_{j,\text{SPT},\ell}(t_\ell)] = \text{Re}[D(\omega_0)]A_{j,\ell} \text{erf } \beta(\omega_0),$$

$$\ell = \text{DGO, RGO}_p, p = 0, 1, \dots, M_j \quad (5)$$

$$t = t_\ell = t_0 + \frac{L_\ell}{c_1}. \quad (6)$$

In obtaining (5) from (A·2), we used the following relation

$$\omega_{s,\ell} = \omega_0 \quad \text{for } t = t_\ell. \quad (7)$$

In the following, the AIRs for adjacent backward transient scattering field components are derived using the TD-SPT [27].

First, we derive the $\text{AIR}_{j,\text{RGO}_0/\text{DGO}}$, $j = \text{E, H}$ of the $\text{RGO}_{p=0}$ (= RGO_0) to the DGO. Applying (A·6) and (A·9) to (5), the $\text{AIR}_{j,\text{RGO}_0/\text{DGO}}$ is given by

$$\begin{aligned} \text{AIR}_{j,\text{RGO}_0/\text{DGO}} &= \frac{\text{Re}[y_{j,\text{SPT},\text{RGO}_0}(t_{\text{RGO}_0})]}{\text{Re}[y_{j,\text{SPT},\text{DGO}}(t_{\text{DGO}})]} \\ &= \frac{\text{Re}[D(\omega_0)]A_{j,\text{RGO}_0} \text{erf } \beta(\omega_0)}{\text{Re}[D(\omega_0)]A_{j,\text{DGO}} \text{erf } \beta(\omega_0)} \\ &= \sqrt{\frac{a(L_> - L_<)}{aL_< + aL_> + 2L_< L_>}} R_{j,11} \quad (8) \end{aligned}$$

where $L_<$ ($L_>$) is a symbol for the smaller (larger) in L_1 (= QQ_0) and L_2 (= Q_0P) in (A·12) (see Fig. 2). The square root term is a divergence factor. The $\text{AIR}_{j,\text{RGO}_0/\text{DGO}}$ is represented by the product of two influence factors, namely the divergence factor and the reflection factor $R_{j,11}$ (see (A·13)).

Second, we derive the $\text{AIR}_{j,\text{RGO}_1/\text{RGO}_0}$, $j = \text{E, H}$ of the $\text{RGO}_{p=1}$ (= RGO_1) to the $\text{RGO}_{p=0}$ (= RGO_0). Applying (A·9) and (A·14) to (5), the $\text{AIR}_{j,\text{RGO}_1/\text{RGO}_0}$ is represented by

$$\begin{aligned} \text{AIR}_{j,\text{RGO}_1/\text{RGO}_0} &= \frac{\text{Re}[y_{j,\text{SPT},\text{RGO}_1}(t_{\text{RGO}_1})]}{\text{Re}[y_{j,\text{SPT},\text{RGO}_0}(t_{\text{RGO}_0})]} \\ &= \frac{\text{Re}[D(\omega_0)]A_{j,\text{RGO}_1} \text{erf } \beta(\omega_0)}{\text{Re}[D(\omega_0)]A_{j,\text{RGO}_0} \text{erf } \beta(\omega_0)} \\ &= \sqrt{\frac{aL_< + aL_> + 2L_< L_>}{aL_< + aL_> + 2L_< L_> + D_1}} \\ &\quad \cdot (T_{j,12}T_{j,21}) \left(\frac{R_{j,2}}{R_{j,11}} \right). \quad (9) \end{aligned}$$

The $\text{AIR}_{j,\text{RGO}_1/\text{RGO}_0}$ is expressed as the product of three influence factors, namely the divergence factor, the transmission factor ($T_{j,12}T_{j,21}$) (see (A·18) and (A·19)), and the reflection factor ($R_{j,2}/R_{j,11}$) (see (A·13) and (A·20)).

Finally, we derive the $\text{AIR}_{j,\text{RGO}_p/\text{RGO}_{p-1}}$, $j = \text{E, H}$, $p = 2, 3, \dots, M_j$ of the RGO_p to the RGO_{p-1} . Applying (A·14) to (5), the $\text{AIR}_{j,\text{RGO}_p/\text{RGO}_{p-1}}$ is given by

$$\begin{aligned} \text{AIR}_{j,\text{RGO}_p/\text{RGO}_{p-1}} &= \frac{\text{Re}[y_{j,\text{SPT},\text{RGO}_p}(t_{\text{RGO}_p})]}{\text{Re}[y_{j,\text{SPT},\text{RGO}_{p-1}}(t_{\text{RGO}_{p-1}})]} \\ &= \frac{\text{Re}[D(\omega_0)]A_{j,\text{RGO}_p} \text{erf } \beta(\omega_0)}{\text{Re}[D(\omega_0)]A_{j,\text{RGO}_{p-1}} \text{erf } \beta(\omega_0)} \\ &= \sqrt{\frac{aL_< + aL_> + 2L_< L_> + D_{p-1}}{aL_< + aL_> + 2L_< L_> + D_p}} \\ &\quad \cdot (R_{j,2}R_{j,22}), \quad p = 2, 3, \dots, M_j. \quad (10) \end{aligned}$$

The $\text{AIR}_{j,\text{RGO}_p/\text{RGO}_{p-1}}$ is expressed as the product of two influence factors, namely the divergence factor and the reflection factor ($R_{j,2}R_{j,22}$) (see (A·20) and (A·21)).

4. Scatterer Information Estimation

4.1 Simulation Model

In this section, we propose a simulation model to be used in the scatterer information estimation method in Sect. 4.3. There are four types of scatterer information, namely the relative permittivity of the surrounding medium 1, the relative permittivity of the coating medium 2 and its thickness, and the radius of a coated metal cylinder.

4.1.1 Assumptions and Notations for Estimation

First, we assume the following (A) to (F) in the scatterer information estimation method.

- (A) The structure of a scatterer is a 2-D coated metal cylinder coated with a uniform dielectric medium layer.
- (B) A pulse source $s(t)$ in (1) and its numerical parameters (ω_0, t_0, d) are known.
- (C) The pulse wave is radiated from a line source Q placed parallel to the central axis of a coated metal cylinder.
- (D) The radius of a scatterer is sufficiently large compared to a wavelength of a central angular frequency ω_0 of a pulse source $s(t)$.
- (E) A line source Q and an observation point P are placed at different locations and a distance L_{DGO} (= QP) between the point Q and the point P is known.
- (F) At the observation point P, the peaks of the response waveforms of the backward transient scattering field components and their arrival times can be observed with high accuracy.

Second, the estimation method uses the following notations (Ā) and (B̄).

- (Ā) Estimates are marked with a caret symbol ($\hat{}$) and are denoted as $\hat{\varepsilon}_{1r}$, $\hat{\varepsilon}_{2r}$, \hat{h} , and \hat{a} .
- (B̄) Numerical parameters and numerical data observed in the response waveforms are marked with an overline

symbol ($\bar{}$) and are denoted as \bar{L}_{DGO} , \bar{t}_0 , \bar{t}_ℓ , and $\text{Re}[y_{j,\text{SPT},\ell}(\bar{t}_\ell)]$.

4.1.2 Simulation Model and Numerical Data of Response Waveforms

Figure 4 (a) shows, as a simulation model for estimating the scatterer information, a diagram of a 2-D coated metal cylinder of radius \hat{a} coated with a coating medium 2 ($\varepsilon_0\hat{\varepsilon}_{2r}, \mu_0$) of thickness \hat{h} . A line source Q and an observation point P are placed at different locations in a surrounding medium 1 ($\varepsilon_0\hat{\varepsilon}_{1r}, \mu_0$). The distance QP between the two points is \bar{L}_{DGO} .

Figure 4 (b) shows an example of numerical data for three sets of response waveforms of the backward transient scattering electric field components calculated from the TD-SPT in (A·1). The peak and arrival time of the DGO are $\text{Re}[y_{E,\text{SPT,DGO}}(\bar{t}_{\text{DGO}})]$ and \bar{t}_{DGO} , respectively. While the peaks and their arrival times of the RGO $_p$, $p = 0, 1$ are $\text{Re}[y_{E,\text{SPT,RGO}_p}(\bar{t}_{\text{RGO}_p})]$ and \bar{t}_{RGO_p} , respectively.

4.2 Derivation of Scatterer Information Estimation Formulae

In this section, we derive estimation formulae for four types of scatterer information ($\hat{\varepsilon}_{1r}, \hat{\varepsilon}_{2r}, \hat{h}, \hat{a}$).

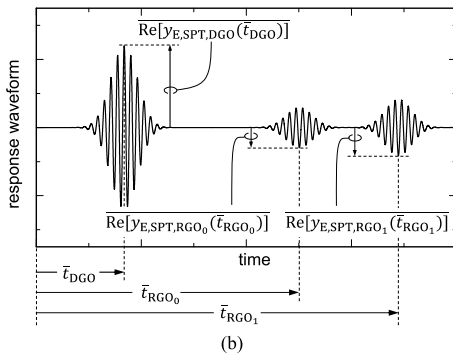
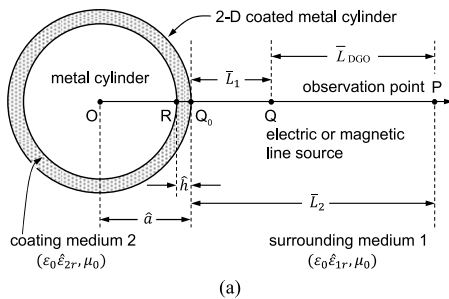


Fig. 4 Simulation model of a scatterer information estimation method. (a) Diagram of a 2-D coated metal cylinder, an electric or magnetic line source Q, an observation point P, a point Q $_0$ on a coating surface of radius \hat{a} , and a point R on a metal surface of radius $\hat{a} - \hat{h}$. (b) An example of numerical data for three sets of peaks of the response waveforms of the backward transient scattering electric field components and their arrival times calculated from the TD-SPT in (A·1).

4.2.1 Estimation Formula $\hat{\varepsilon}_{1r}$ for Relative Permittivity ε_{1r}

Substituting (A·4) into (6) gives

$$\hat{\varepsilon}_{1r} = \left[\frac{c_0}{\bar{L}_{\text{DGO}}} (\bar{t}_{\text{DGO}} - \bar{t}_0) \right]^2 \quad (11)$$

where c_0 is the speed of light in free space (see (A·4)). In the derivation of $\hat{\varepsilon}_{1r}$ in (11), L_{DGO} ($= \text{QP}$) and t_{DGO} , and t_0 are replaced by the numerical data \bar{L}_{DGO} and \bar{t}_{DGO} , and the numerical parameter \bar{t}_0 , respectively.

4.2.2 Estimation Formula $\hat{\varepsilon}_{2r}$ for Relative Permittivity ε_{2r}

Substituting (A·8), (A·11), and (A·12) into (6), we obtain

$$\bar{L}_1 = \frac{c_1}{2} (\bar{t}_{\text{RGO}_0} - \bar{t}_{\text{DGO}}) = \text{QQ}_0 \quad (12)$$

$$\bar{L}_2 = \frac{c_1}{2} (\bar{t}_{\text{RGO}_0} + \bar{t}_{\text{DGO}} - 2\bar{t}_0) = \text{Q}_0\text{P} \quad (13)$$

where \bar{L}_1 (\bar{L}_2) is the distance QQ_0 (Q_0P) from the source point Q (point Q_0) to the point Q_0 (observation point P) (see Fig. 4 (a)).

Then, after substituting (A·13) and (A·18) to (A·20) into (9), we obtain the following formula

$$\hat{\varepsilon}_{2r} = \left[\left(2\bar{\Lambda}_{1/0} + \sqrt{4(\bar{\Lambda}_{1/0})^2 + (\bar{A}_{j,1/0})^2} \right) / \bar{A}_{j,1/0} \right]^2 \hat{\varepsilon}_{1r} \quad (14)$$

$$\bar{\Lambda}_{1/0} = \sqrt{\frac{\hat{a}\bar{L}_< + \hat{a}\bar{L}_> + 2\bar{L}_<\bar{L}_>}{\hat{a}\bar{L}_< + \hat{a}\bar{L}_> + 2\bar{L}_<\bar{L}_> + \bar{D}_1}} \quad (15)$$

$$\bar{D}_{p=1} = \bar{D}_1 = \frac{(\hat{a} + \bar{L}_<)(\hat{a} + \bar{L}_>)(2\hat{h})}{\hat{a} - \hat{h}} \sqrt{\frac{\hat{\varepsilon}_{1r}}{\hat{\varepsilon}_{2r}}} \quad (16)$$

$$\bar{A}_{j,1/0} = \text{AIR}_{j,\text{RGO}_1/\text{RGO}_0} = \frac{\text{Re}[y_{j,\text{SPT,RGO}_1}(\bar{t}_{\text{RGO}_1})]}{\text{Re}[y_{j,\text{SPT,RGO}_0}(\bar{t}_{\text{RGO}_0})]} \quad (17)$$

where $\bar{L}_<$ ($\bar{L}_>$) is a symbol for the smaller (larger) in the numerical data \bar{L}_1 in (12) and \bar{L}_2 in (13). In the derivation of \bar{D}_1 in (16), a , ε_{1r} , h and ε_{2r} , and $L_<$ and $L_>$ are replaced by estimates \hat{a} , $\hat{\varepsilon}_{1r}$, \hat{h} , and $\hat{\varepsilon}_{2r}$, and numerical data $\bar{L}_<$ and $\bar{L}_>$, respectively. The symbols $\bar{\Lambda}_{1/0}$ in (15) and $\bar{A}_{j,1/0}$ in (17) are numerical data of the divergence factor and $\text{AIR}_{j,\text{RGO}_1/\text{RGO}_0}$, respectively. Therefore, by substituting $\hat{\varepsilon}_{1r}$, $\bar{A}_{j,1/0}$, and $\bar{\Lambda}_{1/0}$ into (14), we numerically obtain the estimate of $\hat{\varepsilon}_{2r}$.

While $\hat{\varepsilon}_{2r}$ in (14) can be simplified as follows by approximating $\bar{\Lambda}_{1/0}$ in (15) with one

$$\hat{\varepsilon}_{2r} \sim \left[\left(2 + \sqrt{4 + (\bar{A}_{j,1/0})^2} \right) / \bar{A}_{j,1/0} \right]^2 \hat{\varepsilon}_{1r}. \quad (18)$$

4.2.3 Estimation Formula \hat{h} for Thickness h

Substituting (A·4) and (A·17) into (6), we obtain

$$\hat{h} = \frac{c_0}{2\sqrt{\hat{\varepsilon}_{2r}}}(\bar{t}_{\text{RGO}_1} - \bar{t}_{\text{RGO}_0}). \quad (19)$$

In the derivation of \hat{h} in (19), t_{RGO_0} and t_{RGO_1} are replaced by numerical data \bar{t}_{RGO_0} and \bar{t}_{RGO_1} , respectively. Therefore, by substituting \bar{t}_{RGO_0} , \bar{t}_{RGO_1} , and $\hat{\varepsilon}_{2r}$ into (19), we numerically obtain the estimate of \hat{h} .

4.2.4 Estimation Formula \hat{a} for Radius a

After substituting (A·12), (A·13), (12), and (13) into (8), we obtain the following formula

$$\hat{a} = \frac{2\bar{L}_< \bar{L}_>}{\bar{B}_{j,0/D} - (\bar{L}_< + \bar{L}_>)} \quad (20)$$

$$\bar{B}_{j,0/D} = \frac{\bar{L}_> - \bar{L}_<} {(\bar{A}_{j,0/D})^2} \left(\frac{\sqrt{\hat{\varepsilon}_{2r}} - \sqrt{\hat{\varepsilon}_{1r}}}{\sqrt{\hat{\varepsilon}_{2r}} + \sqrt{\hat{\varepsilon}_{1r}}} \right)^2 \quad (21)$$

$$\bar{A}_{j,0/D} = \overline{\text{AIR}_{j,\text{RGO}_0/\text{DGO}}} = \frac{\text{Re}[y_{j,\text{SPT,RGO}_0}(\bar{t}_{\text{RGO}_0})]}{\text{Re}[y_{j,\text{SPT,DGO}}(\bar{t}_{\text{DGO}})]} \quad (22)$$

where $\bar{A}_{j,0/D}$ is the numerical data of $\overline{\text{AIR}_{j,\text{RGO}_0/\text{DGO}}}$ obtained from Fig. 4 (b). In the derivation of \hat{a} in (20), ε_{1r} and ε_{2r} are replaced by the estimates $\hat{\varepsilon}_{1r}$ and $\hat{\varepsilon}_{2r}$, respectively. Thus, by substituting $\bar{L}_<$, $\bar{L}_>$, $\bar{A}_{j,0/D}$, $\hat{\varepsilon}_{1r}$, and $\hat{\varepsilon}_{2r}$ into (20), we numerically obtain the estimate of \hat{a} .

4.3 Scatterer Information Estimation Method

In this section, we propose a scatterer information estimation method using the estimation formulae which are derived in Sect. 4.2.

In (a) to (j) below, the methods for estimating four types of scatterer information are presented. The symbols ε and I_{MAX} denote on a convergence degree and an upper limit on the number of iterations, respectively.

- Substituting the numerical data \bar{L}_{DGO} and \bar{t}_{DGO} , and the numerical parameter \bar{t}_0 into (11) gives an estimate of $\hat{\varepsilon}_{1r}$.
- Substituting the numerical data $\bar{A}_{j,1/0}$ in (17) and $\hat{\varepsilon}_{1r}$ in (a) into (18) gives an estimate of $\hat{\varepsilon}_{2r} = \hat{\varepsilon}_{2r,I}$. The subscript I is a symbol for the number of iterations.
- By substituting the numerical data \bar{t}_{RGO_0} and \bar{t}_{RGO_1} , and the estimate $\hat{\varepsilon}_{2r,I}$ obtained in (b) into (19), we obtain an estimate of $\hat{h} = \hat{h}_I$.
- Substituting the numerical data $\bar{L}_<$, $\bar{L}_>$, and $\bar{A}_{j,0/D}$ and the estimates $\hat{\varepsilon}_{1r}$ and $\hat{\varepsilon}_{2r,I}$ into (20) gives an estimate of $\hat{a} = \hat{a}_I$.
- We compute \bar{D}_1 in (16) using $\bar{L}_<$, $\bar{L}_>$, $\hat{\varepsilon}_{1r}$, $\hat{\varepsilon}_{2r}$, \hat{h} , and \hat{a} , and then update $\bar{A}_{1/0}$ in (15) using $\bar{L}_<$, $\bar{L}_>$, \hat{a} , and \bar{D}_1 .
- By substituting the estimate $\hat{\varepsilon}_{1r}$ in (a) and the numerical data $\bar{A}_{1/0}$ and $\bar{A}_{j,1/0}$ into (14), we obtain an estimate $\hat{\varepsilon}_{2r} = \hat{\varepsilon}_{2r,I}$ with improved accuracy compared to that in (b).

- To count the number of iterations, we increase the value of I by one. We then obtain new estimates $\hat{h} = \hat{h}_{I+1}$, $\hat{a} = \hat{a}_{I+1}$, and $\hat{\varepsilon}_{2r} = \hat{\varepsilon}_{2r,I+1}$ in (c), (d), and (f). The calculations in (c), (d), (e), and (f) are iterated to improve the accuracy of estimates.
- We use the following equation to determine the convergence degree of the estimates.

$$\Delta \hat{X}_I = \left| \frac{\hat{X}_I - \hat{X}_{I-1}}{\hat{X}_I} \right| < \varepsilon \quad \text{for } X = \varepsilon_{2r}, h, a. \quad (23)$$

In (23), we consider convergence to the set value if the relative difference between the previous estimate \hat{X}_{I-1} and the new estimate \hat{X}_I is less than the convergence degree ε . After saving I in I_{END} , we proceed to (j).

- If I satisfies I_{MAX} , store I_{MAX} in I_{END} and then proceed to (j).
- Output estimates $(\hat{\varepsilon}_{1r}, \hat{\varepsilon}_{2r}, \hat{h}, \hat{a})$ and the number of iterations I_{END} .

4.4 Applicable Conditions of Estimation Method

In this section, we first propose a time-related applicable condition for the scatterer information estimation method. Next, we derive the minimum thickness h_c of a coating medium layer for which the scatterer information estimation method is valid, and propose a new application condition for the thickness of a coating medium layer.

The time t_2 required for a round trip through a coating medium layer of thickness h (see propagation path $Q_0 \rightarrow R \rightarrow Q_0$ in Fig. 2) is given by the following formula using the speed of light c_2 in medium 2.

$$t_2 = \frac{2h}{c_2}, \quad c_2 = \frac{1}{\sqrt{\varepsilon_2 \mu_0}} = \frac{c_0}{\sqrt{\varepsilon_{2r}}}, \quad c_0 = \frac{1}{\sqrt{\varepsilon_0 \mu_0}}. \quad (24)$$

The condition that the peak $\text{Re}[y_{j,\text{SPT,RGO}_p}(t_{\text{RGO}_p})]$ of the response waveform of the p -times reflected GO component in (5) does not combine with the adjacent $p+1$ -times reflected GO component is the applicable condition of the estimation method. Therefore, the applicable condition is that the time t_2 in (24) is greater than or equal to one half of the pulse width ($2t_0$) of a pulse source $s(t)$ in (1) as follows

$$t_2 \geq t_0. \quad (25)$$

Substituting (24) into (25) gives the minimum thickness h_c as follows

$$h_c = \frac{t_0 c_2}{2} = \frac{t_0 c_0}{2\sqrt{\varepsilon_{2r}}}. \quad (26)$$

By using (26), the applicable condition of the estimation method to the thickness h of a coating medium layer is given by

$$h \geq h_c. \quad (27)$$

5. Numerical Results and Discussions

In this section, we first evaluate the accuracy and effectiveness of the TD-SPT and extract numerical data for three sets of backward transient scattering field components needed to estimate the scatterer information. Then, the effectiveness of the scatterer information estimation method is verified by comparing the estimates with the set values. The noise tolerance and convergence characteristics of the estimation method as well as the method of controlling the estimation accuracy are also discussed. In the following calculations, a common factor $D(\omega_0)$ in (A·3), where ω is replaced by ω_0 , is normalized by one ($D(\omega_0) = 1$).

5.1 Accuracy and Effectiveness of TD-SPT and Numerical Data Required for Estimation

Figures 5 (a) and 5 (b) show the response waveforms of the backward transient scattering fields for E- and H-polarizations, respectively. The numerical parameters used in the calculations are given in the caption of Fig. 5. In this case, the time t_2 required for a round trip through the coating medium layer is $t_2 > t_0$, and the thickness h of a coating medium layer is $h > h_c$. Therefore, the numerical parameters used in the calculations in Fig. 5 satisfy the two applicable conditions for the scatterer information estimation method. For visibility of the response waveforms, the vertical axes of the response waveforms shown on the left and right sides of Figs. 5 (a) and 5 (b) are shown by different

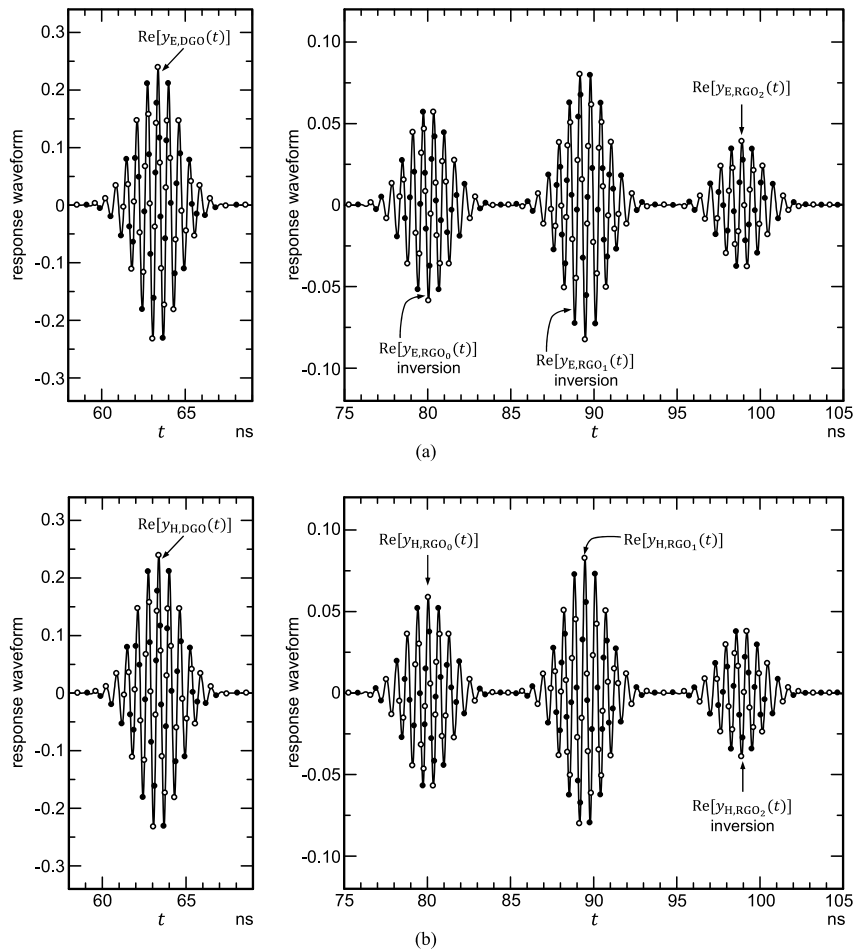


Fig. 5 Response waveforms of backward transient scattering fields for E- and H-polarizations under the condition $\varepsilon_1 < \varepsilon_2$. The numerical parameters used in the calculations are $a = 2.0$ m, $\varepsilon_1 = \varepsilon_0 \varepsilon_{1r}$, $\varepsilon_{1r} = 1$, $\varepsilon_2 = \varepsilon_0 \varepsilon_{2r}$, $\varepsilon_{2r} = 9$, $t_2 = 9.4248 \times 10^{-9}$ s $> t_0 (= 5.0 \times 10^{-9}$ s), and $h = 0.47091$ m ($= 0.23546a$) $> h_c (= 0.24983$ m ($= 0.12491a$)). The source point $Q(\rho_0, \phi_0) = (2.25a, 0.0^\circ)$, the observation point $P(\rho, \phi) = (11.0a, 0.0^\circ)$, and the distance $\bar{L}_{DGO} (= QP) = 8.75a$. The pulse source $s(t)$ used in the calculations is the UWB pulse source shown in Fig. 3.

(a) —: $\text{Re}[y_{E,TD-SPT}(t)]$, $\circ \circ \circ$: $\text{Re}[y_{E,reference}(t)]$, $\bullet \bullet \bullet$: $\text{Re}[y_{E,TD-SPT}(t)]$ when the locations of Q and P are swapped.

(b) —: $\text{Re}[y_{H,TD-SPT}(t)]$, $\circ \circ \circ$: $\text{Re}[y_{H,reference}(t)]$, $\bullet \bullet \bullet$: $\text{Re}[y_{H,TD-SPT}(t)]$ when the locations of Q and P are swapped.

scales.

First, we evaluate the accuracy and effectiveness of the TD-SPT for E-polarization. In Fig. 5 (a), $\text{Re}[y_{E,\text{TD-SPT}}(t)]$ (—) set to $M_E = 2$ (see (A·1)) is in good agreement with the reference solution $\text{Re}[y_{E,\text{reference}}(t)]$ (○ ○ ○) (see (6) in [26]) over the whole region. This allows us to verify the accuracy of the TD-SPT. The computation times of $\text{Re}[y_{E,\text{TD-SPT}}(t)]$ and $\text{Re}[y_{E,\text{reference}}(t)]$ are 0.0128 s and 0.2425 s, respectively. The computation speed ratio of the TD-SPT to the reference solution is 18.95, thereby confirming the effectiveness of the TD-SPT. In $\text{Re}[y_{E,\text{TD-SPT}}(t)]$ in (A·1), the calculations when the locations of a source point Q and an observation point P are swapped are indicated by black circles (●●●). Since the black circles (●●●) are identical to the solid line (—), we can numerically confirm that the TD-SPT satisfies the reciprocity principle [30].

Next, the accuracy and effectiveness of the TD-SPT for H-polarization, shown in Fig. 5(b), can be discussed in the same way as those for E-polarization described above. In this way, we can confirm the accuracy and effectiveness of TD-SPT for H-polarization.

Table 1 shows the numerical data for the peaks of DGO and RGO_p , $p = 0, 1$ for both E- and H-polarizations and their arrival times. We observe that there are two relationships between the peaks for E-polarization and those for H-polarization, as follows

$$\overline{\text{Re}[y_{E,\text{SPT,DGO}}(\bar{t}_{\text{DGO}})]} = \overline{\text{Re}[y_{H,\text{SPT,DGO}}(\bar{t}_{\text{DGO}})]} \quad (28)$$

$$\overline{\text{Re}[y_{E,\text{SPT,RGO}_p}(\bar{t}_{\text{RGO}_p})]} = -\overline{\text{Re}[y_{H,\text{SPT,RGO}_p}(\bar{t}_{\text{RGO}_p})]}. \quad (29)$$

The sign inversions for the peaks of RGO_p , $p = 0, 1$ due to the polarization difference shown in (29) can be observed in Fig. 5. The reason for these inversions is that $R_{E,11} = -R_{H,11}$ for RGO_0 and $R_{E,2} = -R_{H,2}$ for RGO_1 .

The reference solution $\text{Re}[y_{j,\text{reference}}(t)]$, $j = E, H$,

which is expressed in integral form, is computed numerically using the fast Fourier transform (FFT) numerical code [31]. Therefore, it is difficult to extract and calculate the peaks of the backward transient scattering field components and their arrival times from $\text{Re}[y_{j,\text{reference}}(t)]$. In contrast, the peaks of the backward transient scattering field components and their arrival times can be calculated from (5) and (6), respectively. Also, the inversion phenomena for the peaks of the response waveforms can be analytically interpreted from (5) in conjunction with (A·6), (A·9), and (A·14). From the above advantages over the reference solution, we can confirm the practicality of TD-SPT.

5.2 Effectiveness of Scatterer Information Estimation Method

In this section, we verify the effectiveness of the scatterer information estimation method proposed in Sect. 4.3 by substituting specific numerical values into the estimation formulae for four types of scatterer estimation ($\hat{\varepsilon}_{1r}, \hat{\varepsilon}_{2r}, \hat{h}, \hat{a}$) in the simulation model shown in Fig. 4 (a). The numerical parameters used in the simulation experiments are the numerical data for three sets of backward transient scattering field components listed in Table 1 and the distance \bar{L}_{DGO} (= QP) given in the caption of Fig. 5. The convergence degree and the upper limit of the number of iterations are set to $\varepsilon = 1.0 \times 10^{-9}$ and $I_{\text{MAX}} = 100$, respectively.

First, we validate the effectiveness of the estimation method for E-polarization. Table 2 shows the set values, estimates, and estimation errors for the four types of scatterer information. The following equation was used to calculate the estimation errors.

$$\text{estimation error} = \left| \frac{\bar{X} - \hat{X}}{\bar{X}} \right| \quad \text{for } X = \varepsilon_{1r}, \varepsilon_{2r}, h, a. \quad (30)$$

Table 1 Numerical data for three sets of response waveforms of the backward transient scattering field components for both E- and H-polarizations calculated from (5) and (6). The numerical parameters used in the simulation experiments are the same as those used in Fig. 5. Here, the thickness h is 0.47091 m (= 0.23546 a).

field components	peaks	arrival times
DGO	$\overline{\text{Re}[y_{E,\text{SPT,DGO}}(\bar{t}_{\text{DGO}})]} = +0.2390252779110931$ $\overline{\text{Re}[y_{H,\text{SPT,DGO}}(\bar{t}_{\text{DGO}})]} = +0.2390252779110931$	$\bar{t}_{\text{DGO}} = 0.6337371666092792 \times 10^{-7}$ s
RGO_0	$\overline{\text{Re}[y_{E,\text{SPT,RGO}_0}(\bar{t}_{\text{RGO}_0})]} = -0.5871699985606935 \times 10^{-1}$ $\overline{\text{Re}[y_{H,\text{SPT,RGO}_0}(\bar{t}_{\text{RGO}_0})]} = +0.5871699985606935 \times 10^{-1}$	$\bar{t}_{\text{RGO}_0} = 0.8005192142119303 \times 10^{-7}$ s
RGO_1	$\overline{\text{Re}[y_{E,\text{SPT,RGO}_1}(\bar{t}_{\text{RGO}_1})]} = -0.8248377248296151 \times 10^{-1}$ $\overline{\text{Re}[y_{H,\text{SPT,RGO}_1}(\bar{t}_{\text{RGO}_1})]} = +0.8248377248296151 \times 10^{-1}$	$\bar{t}_{\text{RGO}_1} = 0.8947669938196241 \times 10^{-7}$ s

Table 2 Set values, estimates, and estimation errors of four types of scatterer information for E- and H-polarizations. The numerical parameters used in the simulation experiments are the same as those used in Fig. 5.

scatterer information	set values	estimates	estimation errors
ε_{1r}	$\bar{\varepsilon}_{1r} = 1.0000000000000000$	$\hat{\varepsilon}_{1r} = 1.0000000000000000$	0.00000
ε_{2r}	$\bar{\varepsilon}_{2r} = 9.0000000000000000$	$\hat{\varepsilon}_{2r} = 9.0000000000000568$	0.63159×10^{-14}
h	$\bar{h} = 0.4709128918171183$ m	$\hat{h} = 0.4709128918171170$ m	0.27112×10^{-14}
a	$\bar{a} = 2.0000000000000000$ m	$\hat{a} = 1.999999999999858$ m	0.74385×10^{-14}

Since the number of iterations I_{END} is six, three types of estimates ($\hat{\varepsilon}_{2r}, \hat{h}, \hat{a}$) satisfy the convergence condition. From the high accuracy of four types of estimates ($\hat{\varepsilon}_{1r}, \hat{\varepsilon}_{2r}, \hat{h}, \hat{a}$) in Table 2, we can confirm the effectiveness of the estimation method for E-polarization in Sect. 4.3. In the simulation experiment, the estimates for the four types of scatterer information when the locations of a source point Q and an observation point P were swapped were identical to those in Table 2. The reason for the identical estimates is that the values of the numerical data listed in Table 1 and the distance \bar{L}_{DGO} do not change when the locations of the point Q and the point P are swapped.

Next, the effectiveness of the estimation method for H-polarization can be validated in the same way as for E-polarization, as described above. Since the estimation formulae for scatterer information derived in Sect. 4.2 are not affected by the sign of the AIRs, we obtained estimates and estimation errors identical to those in Table 2. Thus, we can numerically confirm the effectiveness of the estimation method for H-polarization in Sect. 4.3 and the polarization independence of the estimates.

5.3 Noise Tolerance of Estimation Method

In this section, we discuss the noise tolerance of the estimation method proposed in Sect. 4.3 when noise is added to the response waveforms of the backward transient scattering fields for E- and H-polarizations shown in Figs. 5 (a) and 5 (b).

The numerical parameters used in the calculations are shown in the caption of Fig. 5. The convergence degree and the upper limit of the number of iterations were set to $\varepsilon = 1.0 \times 10^{-9}$ and $I_{\text{MAX}} = 100$, respectively. In the simulation experiments, noise was added to the signal data of the response waveform to generate new signal data mixed with the response waveform and noise. Specifically, the observation time range of $58 \text{ ns} \leq t \leq 105 \text{ ns}$ shown in Fig. 5 was divided by a step size of $\Delta t = 4.7 \times 10^{-13} \text{ s}$ to generate 10^5 pairs of noise-added signal data.

As a measure of the signal-to-noise power ratio, we used the following signal-to-noise ratio (SNR)

$$\text{SNR} = 20 \log_{10} \frac{\text{Signal}_{\text{RMS}}}{\text{Noise}_{\text{RMS}}} \quad (31)$$

where $\text{Signal}_{\text{RMS}}$ is the strength of the response waveform signal and denotes the root mean square (RMS) of the amplitude values of the response waveform signal after removing the no-signal region. In this section, it is assumed that the noise is generated by the surface roughness at points Q_0 and R shown in Fig. 4 (a). The noise was modeled as an additive white Gaussian noise (AWGN) [32]. $\text{Noise}_{\text{RMS}}$ is the noise strength, which denotes the RMS of the AWGN amplitude values. To obtain an arbitrary SNR, the $\text{Noise}_{\text{RMS}}$ was superimposed on the $\text{Signal}_{\text{RMS}}$ to generate noise-added signal data.

First, we discuss the noise tolerance of the estimation method for E-polarization. Figure 6 shows the estimation

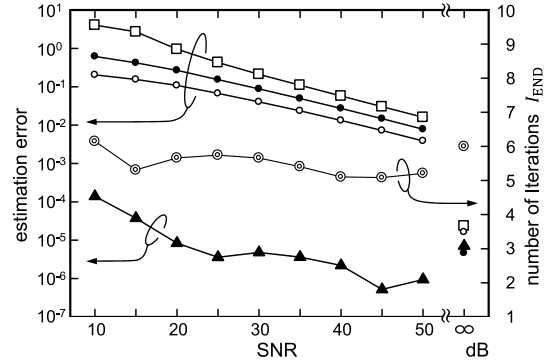


Fig. 6 Estimation errors for four types of estimates ($\hat{\varepsilon}_{1r}, \hat{\varepsilon}_{2r}, \hat{h}, \hat{a}$) for E- and H- polarizations when the SNR is varied under the condition that the convergence degree is set to $\varepsilon = 1 \times 10^{-9}$ and the number of significant digits of the numerical data for the arrival time is set to 8. The numerical parameters used in the simulation experiments are the same as those used in Fig. 5. $\blacktriangle \blacktriangle \blacktriangle$: $\hat{\varepsilon}_{1r}$, $\bullet \bullet \bullet$: $\hat{\varepsilon}_{2r}$, $\circ \circ \circ$: \hat{h} , $\square \square \square$: \hat{a} , $\odot \odot \odot$: I_{END} .

errors and the number of iterations I_{END} for four types of estimates ($\hat{\varepsilon}_{1r}, \hat{\varepsilon}_{2r}, \hat{h}, \hat{a}$) as the SNR is varied from 10 to 50. The results for an SNR value of ∞ (no noise) are also included as a reference to compare the noise tolerance. The values of the estimation errors and I_{END} are the averages over 5×10^3 trials, at each SNR.

When the SNR value is ∞ , the estimation errors for the estimates ($\hat{\varepsilon}_{1r}, \hat{\varepsilon}_{2r}, \hat{h}, \hat{a}$) are approximately 10^{-5} . Compared to the estimation errors for the estimates ($\hat{\varepsilon}_{1r}, \hat{\varepsilon}_{2r}, \hat{h}, \hat{a}$) shown in Table 2, the errors shown in Fig. 6 are significantly different. This difference is due to the fact that the significant digits of the arrival time used in the estimation in Table 2 are 16 digits, while the significant digits of the arrival time used in the estimation in Fig. 6 are 8 digits. Therefore, when the estimates ($\hat{\varepsilon}_{2r}, \hat{h}, \hat{a}$) are obtained from the noise-added response waveform signals, the estimation errors of these estimates deteriorate from about 10^{-5} . On the other hand, the estimate $\hat{\varepsilon}_{1r}$ is obtained by substituting \bar{L}_{DGO} , \bar{t}_{DGO} , and \bar{t}_0 into (11). The estimation accuracy of $\hat{\varepsilon}_{1r}$ depends on \bar{t}_{DGO} and not on the convergence degree ε or the I_{END} . Therefore, when the estimate $\hat{\varepsilon}_{1r}$ is obtained from the noise-added signal data, the estimation errors remain around 10^{-5} .

Figure 6 shows that the estimation errors of $\hat{\varepsilon}_{1r}$ are about 10^{-6} and 10^{-4} for SNR values of 50 and 10, respectively, and are nearly linear. The estimation errors of the estimates ($\hat{\varepsilon}_{2r}, \hat{h}, \hat{a}$) are about 10^{-2} and $2 \times 10^{-1} \sim 4 \times 10^0$ for SNR values of 50 and 10, respectively, and are linear. The I_{END} is independent of the SNR and is about 6. The estimation errors of the estimates ($\hat{\varepsilon}_{1r}, \hat{\varepsilon}_{2r}, \hat{h}, \hat{a}$) for H-polarization and the calculations for I_{END} are almost the same as those for E-polarization.

From the above discussions, the estimation method proposed in Sect. 4.3 has the following noise tolerance when the significant digits of the time increments and the convergence degree are set to 8 digits and $\varepsilon = 1.0 \times 10^{-9}$, respectively. The estimates ($\hat{\varepsilon}_{2r}, \hat{h}, \hat{a}$) for SNRs of ∞ , 50, 30, and 10, the estimation errors are approximately 10^{-5} , 10^{-2} , 10^{-1} , and $2 \times 10^{-1} \sim 4 \times 10^0$, respectively. On the other hand, the

Table 3 Numerical data for three sets of response waveforms of the backward transient scattering field components for both E- and H-polarizations calculated from (5) and (6). The numerical parameters used in the simulation experiments are the same as those used in Fig. 5, except for the thickness h of a coating medium 2. Here, the thickness h is 0.79113 m ($= 0.39557a$).

field components	peaks	arrival times
DGO	$\text{Re}[y_{E,SPT,DGO}(\bar{t}_{DGO})] = +0.2390252779110931$ $\text{Re}[y_{H,SPT,DGO}(\bar{t}_{DGO})] = +0.2390252779110931$	$\bar{t}_{DGO} = 0.6337371666092792 \times 10^{-7}$ s
RGO ₀	$\text{Re}[y_{E,SPT,RGO_0}(\bar{t}_{RGO_0})] = -0.5871699985606935 \times 10^{-1}$ $\text{Re}[y_{H,SPT,RGO_0}(\bar{t}_{RGO_0})] = +0.5871699985606935 \times 10^{-1}$	$\bar{t}_{RGO_0} = 0.8005192142119303 \times 10^{-7}$ s
RGO ₁	$\text{Re}[y_{E,SPT,RGO_1}(\bar{t}_{RGO_1})] = -0.7731026089010065 \times 10^{-1}$ $\text{Re}[y_{H,SPT,RGO_1}(\bar{t}_{RGO_1})] = +0.7731026089010065 \times 10^{-1}$	$\bar{t}_{RGO_1} = 0.9588554839528558 \times 10^{-7}$ s

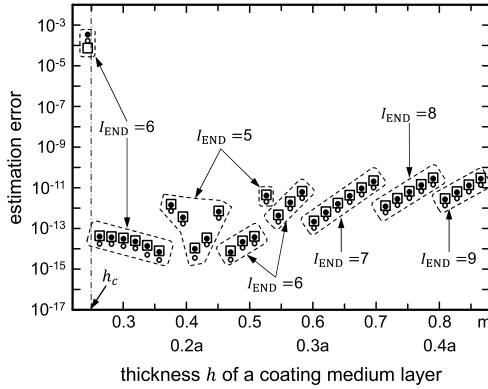


Fig. 7 Estimation errors for three types of estimates ($\hat{\epsilon}_{2r}$, \hat{h} , \hat{a}) for E- and H-polarizations when the thickness h of a coating medium 2 is varied under the condition that the convergence degree ϵ is set to $\epsilon = 1 \times 10^{-9}$. The numerical parameters used in the simulation experiments are the same as those used in Fig. 5, except for the thickness h . The minimum thickness h_c in (26) is 0.24983 m ($= 0.12491a$). $\bullet \bullet \bullet$: $\hat{\epsilon}_{2r}$, $\circ \circ \circ$: \hat{h} , $\square \square \square$: \hat{a} .

estimation errors of the estimate $\hat{\epsilon}_{1r}$ for SNRs of ∞ , 50, 30, and 10 are approximately 10^{-5} , 10^{-6} , 10^{-5} , and 10^{-4} , respectively.

5.4 Convergence Characteristics of Scatterer Information Estimation Method

In this section, we test the convergence characteristics of the scatterer information estimation method as the thickness h of a coating medium 2 is varied. The estimation accuracy of the estimate $\hat{\epsilon}_{1r}$ does not depend on the convergence degree ϵ and the number of iterations I_{END} . In the following, we will discuss the convergence properties of the estimation method by calculating the estimation errors and the number of iterations I_{END} for the three types of scatterer information estimates ($\hat{\epsilon}_{2r}$, \hat{h} , \hat{a}).

Figure 7 shows the estimation errors of the scatterer information for E-polarization and the number of iterations I_{END} for different thicknesses h under the condition that the convergence degree is set to $\epsilon = 1 \times 10^{-9}$. The numerical parameters used in the simulation experiments are the numerical data of three sets of backward transient scattering field components obtained analytically from TD-SPT and the distance \bar{L}_{DGO} ($= QP$) given in the caption of Fig. 5. The thickness h was set to range from 0.24487 m ($= 0.12244a$) to 0.86648 m ($= 0.43324a$), including the minimum thickness h_c ($= 0.24983$ m ($= 0.12491a$)) in (26).

From Fig. 7, when the thickness h satisfies the applicable condition in (27) ($h \geq h_c$), the estimation errors are distributed in the range of 10^{-14} to 10^{-10} , and the I_{END} varies from 5 to 9. The thickness with minimum errors was $h = 0.47091$ m ($= 0.23546a$), and the thickness with maximum errors was $h = 0.79113$ m ($= 0.39557a$). When the thickness h did not satisfy the applicable condition in (27) ($h < h_c$), the estimation errors were distributed in the range of 10^{-4} to 10^{-3} , and the I_{END} was 6. The estimation errors of the scatterer information for the H-polarization and the I_{END} were exactly the same as those for the E-polarization.

From the above discussions, it is estimated that for E- and H-polarizations, under the application conditions of Sect. 4.4, when the convergence degree is set to $\epsilon = 1 \times 10^{-9}$ and the estimation method of Sect. 4.3 is used, the estimates ($\hat{\epsilon}_{2r}$, \hat{h} , \hat{a}) converge to an accuracy between 10^{-14} and 10^{-10} with a number of iterations of one digit.

5.5 Method for Controlling the Estimation Accuracy

The accuracy of the estimate $\hat{\epsilon}_{1r}$ is independent of the convergence degree ϵ and the number of iterations I_{END} . In this section, we will discuss how to control the estimation accuracy of three types of scatterer information estimates ($\hat{\epsilon}_{2r}$, \hat{h} , \hat{a}). For the simulation experiments, we selected two values of $h = 0.47091$ m ($= 0.23546a$) and $h = 0.79113$ m ($= 0.39557a$) for the thickness of a coating medium 2, which gave the minimum and maximum estimation errors in Fig. 7. Tables 1 and 3 show the numerical data of three sets of backward transient scattering field components for both E- and H-polarizations for thicknesses $h = 0.47091$ m and $h = 0.79113$ m, respectively.

Figure 8 shows the estimation errors of the estimates ($\hat{\epsilon}_{2r}$, \hat{h} , \hat{a}) and the I_{END} for E-polarization for different degrees of convergence ϵ under the condition that the thicknesses are set to $h = 0.47091$ m and $h = 0.79113$ m, respectively, as well as auxiliary lines representing their evolution.

First, the case $h = 0.47091$ m is discussed. We observe that when the value of ϵ is decreased (increased), the errors become smaller (larger). If the I_{END} is the same, there is no change in the error when the value of ϵ is changed. Referring to the dashed auxiliary line (-----), the errors tend to decrease by one order of magnitude when the ϵ is decreased by one order of magnitude. The calculations of the estimation errors for the estimates ($\hat{\epsilon}_{2r}$, \hat{h} , \hat{a}) for H-polarization were exactly the same as for E-polarization. From the above

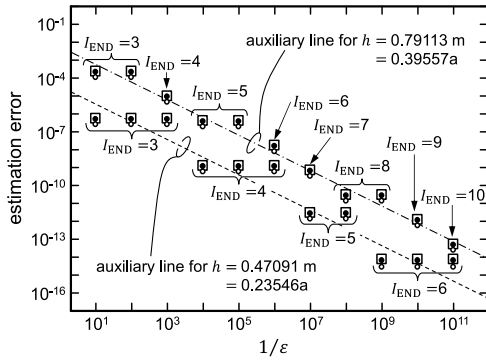


Fig. 8 Estimation errors for three types of estimates ($\hat{\epsilon}_{2r}$, \hat{h} , \hat{a}) for E- and H-polarizations when the convergence degree ϵ is varied under the condition of the fixed thickness h of a coating medium 2. The numerical parameters used in the simulation experiments are the same as those used in Fig. 5, except for the thickness h . Here, the thicknesses are set to $h = 0.47091$ m ($= 0.23546a$) and $h = 0.79113$ m ($= 0.39557a$), respectively. $\bullet\bullet\bullet$: $\hat{\epsilon}_{2r}$, $\circ\circ\circ$: \hat{h} , $\square\square\square$: \hat{a} .

discussions, we can confirm that the estimation accuracy of the estimates ($\hat{\epsilon}_{2r}$, \hat{h} , \hat{a}) for both E- and H-polarizations can be controlled by varying the value of the ϵ .

Next, the case $h = 0.79113$ m is discussed. The trend of the changes in the estimation errors of the estimates ($\hat{\epsilon}_{2r}$, \hat{h} , \hat{a}) for $1/\epsilon$ is shown by the single dash-dotted auxiliary line (— · — ·). Compared to the broken auxiliary line (— · — ·), the single dash-dotted auxiliary line (— · — ·) has an almost identical slope, with the errors increasing by about 10^2 . The trend of the error variations in the estimates ($\hat{\epsilon}_{2r}$, \hat{h} , \hat{a}) for H-polarization was the same as for E-polarization. The same slope of the two auxiliary lines indicates that the estimation accuracy of the estimates ($\hat{\epsilon}_{2r}$, \hat{h} , \hat{a}) for both E- and H-polarizations for $h = 0.79113$ m can be controlled by changing the value of the ϵ .

From the above discussions, we can confirm the effectiveness of the control method for the estimation accuracy.

6. Conclusions

In this paper, we have proposed the scatterer information estimation method using numerical data for the response waveform of a backward transient scattering field for both E- and H-polarizations when a 2-D coated metal cylinder is selected as a scatterer. It was assumed that a line source and an observation point were placed at different locations.

Specifically, the four types of scatterer information estimation formulae, namely the relative permittivity of a surrounding medium, the relative permittivity of a coating medium layer and its thickness, and the radius of a coated metal cylinder, have been derived from the AIRs using the TD-SPT. We obtained the estimates by substituting the numerical data for three sets of the peaks of the response waveforms of the backward transient scattering field components and their arrival times and the numerical data of the distance between the source point and the observation point into the estimation formulae, followed by the iterative calculations.

Furthermore, we derived the minimum thickness of a

coating medium layer for which the estimation method is valid, and proposed two kinds of applicable conditions for the estimation method. By comparing the estimates with the set values, we verified the effectiveness of the scatterer information estimation method proposed in this paper. We also discussed the noise tolerance and convergence characteristics of the estimation method and the method of controlling the estimation accuracy.

In the future, a new method for estimating scatterer information when a line source and an observation point are placed at the same location will be investigated.

References

- [1] J.B. Keller, "Diffraction by a convex cylinder," I.R.E. Trans. Antennas Propagat., vol.AP-4, no.3, pp.312–321, July 1956. DOI: 10.1109/tap.1956.1144427
- [2] P.H. Pathak, "An asymptotic analysis of the scattering of plane waves by a smooth convex cylinder," Radio Science, vol.14, no.3, pp.419–435, May-June 1979.
- [3] P.H. Pathak, W.D. Burnside, and R.J. Marhefka, "A uniform GTD analysis of the diffraction of electromagnetic waves by a smooth convex surface," IEEE Trans. Antennas Propagat., vol.AP-28, no.5, pp.631–642, Sept. 1980. DOI: 10.1109/tap.1980.1142396
- [4] R.C. Hansen, ed., Geometrical Theory of Diffraction, IEEE Press, New York, 1981.
- [5] N. Wang, "Electromagnetic scattering from a dielectric-coated circular cylinder," IEEE Trans. Antennas Propagat., vol.AP-33, no.9, pp.960–963, Sept. 1985. DOI: 10.1109/TAP.1985.1143696
- [6] G.L. James, ed., Geometrical Theory of Diffraction for Electromagnetic Waves, 3rd ed., Peter Peregrinus, London, 1986. DOI: 10.1049/pbew001e
- [7] H.-T. Kim and N. Wang, "UTD solution for electromagnetic scattering by a circular cylinder with thin lossy coatings," IEEE Trans. Antennas Propagat., vol.37, no.11, pp.1463–1472, Nov. 1989. DOI: 10.1109/8.43566
- [8] P. Hussar and R. Albus, "On the asymptotic frequency behavior of uniform GTD in the shadow region of a smooth convex surface," IEEE Trans. Antennas Propagat., vol.39, no.12, pp.1672–1680, Dec. 1991.
- [9] L.B. Felsen and N. Marcuvitz, eds., Radiation and Scattering of Waves, IEEE Press, New York, 1994. DOI: 10.1109/9780470546307
- [10] T.B.A. Senior and J.L. Volakis, eds., Approximate Boundary Conditions in Electromagnetics, IEE, London, 1995. DOI: 10.1049/pbew041e
- [11] P.E. Hussar, "A uniform GTD treatment of surface diffraction by impedance and coated cylinders," IEEE Trans. Antennas Propagat., vol.46, no.7, pp.998–1008, July 1998. DOI: 10.1109/8.704801
- [12] H. Vollmer and E.J. Rothwell, "Resonance series representation of the early-time field scattered by a coated cylinder," IEEE Trans. Antennas Propagat., vol.52, no.8, pp.2186–2190, Aug. 2004. DOI: 10.1109/TAP.2004.832331
- [13] T. Ida and T. Ishihara, "Novel high-frequency asymptotic solutions in the transition regions near geometrical boundaries and near caustics for scattering by a dielectric cylinder," IEICE Trans. Electron., vol.E87-C, no.9, pp.1550–1559, Sept. 2004.
- [14] T. Ida and T. Ishihara, "Novel high-frequency uniform asymptotic solution for scattered field by a conducting cylinder," IEICE Trans. Electron. (Japanese Edition), vol.J87-C, no.10, pp.754–767, Oct. 2004.
- [15] T. Ida, T. Ishihara, and K. Goto, "Frequency-domain and time-domain novel uniform asymptotic solutions for scattered fields by an impedance cylinder and a dielectric cylinder," IEICE Trans. Electron., vol.E88-C, no.11, pp.2124–2135, Nov. 2005. DOI: 10.1093/ietele/e88-c.11.2124

- [16] J. Sun and L.-W. Li, “Dispersion of waves over a PEC cylinder coated with two-layer lossy dielectric materials,” *IEEE Trans. Antennas Propagat.*, vol.55, no.3, pp.877–881, March 2007. DOI: 10.1109/TAP.2007.891856
- [17] G. Roqueta, L. Jofre, and M.Q. Feng, “Analysis of the electromagnetic signature of reinforced concrete structures for nondestructive evaluation of corrosion damage,” *IEEE Trans. Instrum. Meas.*, vol.61, no.4, pp.1090–1098, April 2012. DOI: 10.1109/TIM.2011.2174106
- [18] M. Nishimoto and Y. Naka, “Analysis of transient scattering by a metal cylinder covered with inhomogeneous lossy material for nondestructive testing,” *IEICE Trans. Electron.*, vol.E101-C, no.1, pp.44–47, Jan. 2018. DOI: 10.1587/transele.E101.C.44
- [19] M. Nishimoto, B.P.A. Rohman, Y. Naka, and K. Ogata, “Corrosion state estimation of rebar in reinforced concrete using ultra-wideband radar,” *IEICE Trans. Electron. (Japanese Edition)*, vol.J104-C, no.11, pp.319–325, Nov. 2021. DOI: 10.14923/transelej.2021JCI0001
- [20] K. Hagiwara, K. Goto, S. Tokumaru, L. Okada, and Y. Takeno, “Novel time-domain asymptotic-numerical solutions for transient scattered electric field from a coated cylinder covered with a thick dielectric medium,” *IEICE Electron. Express*, vol.14, no.5, 20170085, pp.1–10, March 2017. DOI: 10.1587/elex.14.20170085
- [21] T. Kawano and K. Goto, “Novel time-domain asymptotic-numerical solution for forward transient scattered magnetic field from a coated metal cylinder,” *IEICE Electron. Express*, vol.17, no.18, 20200246, pp.1–5, Sept. 2020. DOI: 10.1587/elex.17.20200246
- [22] T. Kawano and K. Goto, “Novel time-domain asymptotic-numerical solution for backward transient scattered magnetic field from a coated metal cylinder,” *IEICE Electron. Express*, vol.18, no.2, 20200399, pp.1–6, Jan. 2021. DOI: 10.1587/elex.18.20200399
- [23] T. Kawano and K. Goto, “Interpretation method of inversion phenomena on backward transient scattered field components by a coated metal cylinder,” *IEICE Trans. Electron.*, vol.E105-C, no.9, pp.389–397, Sept. 2022. DOI: 10.1587/transele.2021ECP5051
- [24] K. Goto and T. Kawano, “A study on the polarization dependence of backward transient scattering by a two-dimensional coated conducting cylinder using the TD-SPT,” *Proc. ICEAA 2022*, p.26, Cape Town, Sept. 2022. DOI: 10.1109/ICEAA49419.2022.9900030
- [25] T. Kawano and K. Goto, “A novel time-domain asymptotic solution for a backward transient scattered electric field by a coated metal cylinder,” *Proc. ICEAA 2022*, pp.27–30, Cape Town, Sept. 2022. DOI: 10.1109/ICEAA49419.2022.9899979
- [26] K. Goto and T. Kawano, “An interpretation method on amplitude intensities for response waveforms of backward transient scattered field components by a 2-D coated metal cylinder,” *IEICE Trans. Electron.*, vol.E106-C, no.4, pp.118–126, April 2023. DOI: 10.1587/transele.2022REP0001
- [27] K. Goto, T. Kawano, M. Kato, and H. Koriyama, “Estimation method of scatterer information using the response waveform of a backward transient scattered magnetic field by the TD-SPT—Case where source and observation points are located at different locations—,” *The Papers of Technical Meeting on Electromagnetic Theory, IEE Japan*, EMT-22-34, pp.19–27, June 2022.
- [28] M. Abramowitz and I.A. Stegun, eds., *Handbook of Mathematical Functions*, 10th ed., Dover, New York, 1972.
- [29] Federal Communications Commission (FCC), ed., *First report and order: Revision of part 15 of the commission’s rules regarding ultra-wideband transmission systems*, FCC 02-48, Washington, D.C., April 2002.
- [30] C.A. Balanis, ed., *Advanced Engineering Electromagnetics*, John Wiley & Sons, New Jersey, 1989.
- [31] E.O. Brigham, ed., *The Fast Fourier Transform*, Prentice-Hall, New Jersey, 1974.
- [32] Y. Kamiyama, ed., *Digital Wireless Communication Technologies with MATLAB*, Corona Publishing, Tokyo, 2020 (in Japanese).
- [33] R.G. Kouyoumjian and P.H. Pathak, “A uniform geometrical theory of diffraction for an edge in a perfectly conducting surface,” *Proc.*

IEEE, vol.62, no.11, pp.1448–1461, Nov. 1974.

Appendix: Time-Domain Saddle-Point Technique (TD-SPT)

A TD-SPT on the z -component of a backward transient scattering field for both E- and H-polarizations $y_j(\rho_0, \phi_0, \rho \neq \rho_0, \phi = \phi_0; t) = y_j(t)$, $j = E, H$ from a coated metal cylinder is given by [23]

$$y_j(t) \sim y_{j,\text{TD-SPT}}(t) = y_{j,\text{SPT,DGO}}(t) + \sum_{p=0}^{M_j} y_{j,\text{SPT,RGO}_p}(t), \quad j = E, H. \quad (\text{A}\cdot 1)$$

In (A·1), $y_{j,\text{SPT,DGO}}(t)$ and $y_{j,\text{SPT,RGO}_p}(t)$ are the DGO and RGO solutions, respectively, and are given by [23]

$$y_{j,\text{SPT},\ell}(t) = D(\omega_{s,\ell}) A_{j,\ell} \text{Re}[\text{erf} \beta(\omega_{s,\ell})] s \left(t - \frac{L_\ell}{c_1} \right), \quad \ell = \text{DGO}, \text{RGO}_p, \quad \text{for } \frac{L_\ell}{c_1} \leq t \leq 2t_0 + \frac{L_\ell}{c_1} \quad (\text{A}\cdot 2)$$

where $D(\omega)$ and c_1 denote a common factor and the speed of light in a surrounding medium 1, respectively, and $\omega_{s,\ell}$ is a saddle point [23]. The notations $\text{erf } z$ and $s(t)$ denote the error function in (4) [28] and the pulse source in (1), respectively. The symbol $\beta(\omega)$ is defined in (3) and M_j is the number of truncated terms in the RGO series.

$$D(\omega) = \sqrt{\frac{c_1}{8\pi\omega}} \exp(i\pi/4) \quad (\text{A}\cdot 3)$$

$$c_1 = \frac{1}{\sqrt{\epsilon_{1\mu_0}}} = \frac{c_0}{\sqrt{\epsilon_{1r}}}, \quad c_0 = \frac{1}{\sqrt{\epsilon_0\mu_0}} \quad (\text{A}\cdot 4)$$

$$\omega_{s,\ell} = \omega_0 - i \frac{1}{2d^2} \left(t - t_0 - \frac{L_\ell}{c_1} \right), \quad \ell = \text{DGO}, \text{RGO}_p. \quad (\text{A}\cdot 5)$$

The notations $D(\omega_{s,\ell}) A_{j,\ell} \text{Re}[\text{erf} \beta(\omega_{s,\ell})]$ and L_ℓ denote the amplitude and distance functions of $y_{j,\text{SPT},\ell}(t)$ in (A·2), respectively.

A.1 Symbols $A_{j,\text{DGO}}$ and L_{DGO} of DGO in (A·2)

The symbols $A_{j,\text{DGO}}$ and L_{DGO} of DGO propagating along the path $Q \rightarrow P$ from a source point Q to an observation point P (see Fig. 2) are given by [23]

$$A_{j,\text{DGO}} = \hat{A}_{j,\text{DGO}} \quad (\text{A}\cdot 6)$$

$$\hat{A}_{j,\text{DGO}} = \sqrt{\frac{1}{L_{\text{DGO}}}} \quad (\text{A}\cdot 7)$$

$$L_{\text{DGO}} = |\rho_0 - \rho| = \text{QP} \quad (\text{A}\cdot 8)$$

where $\hat{A}_{j,\text{DGO}}$ is a divergence factor of DGO [33].

A.2 Symbols A_{j,RGO_0} and L_{RGO_0} of RGO_0 in (A·2)

The symbols A_{j,RGO_0} and L_{RGO_0} of RGO_0 propagating along the path $Q \rightarrow Q_0 \rightarrow P$, which is emitted at the point Q and reflected at the point Q_0 on a coating surface defined by radius $\rho = a$ before arriving at the point P (see Fig. 2), are given by [23]

$$A_{j,\text{RGO}_0} = \hat{A}_{j,\text{RGO}_0} R_{j,11} \quad (\text{A} \cdot 9)$$

$$\hat{A}_{j,\text{RGO}_0} = \sqrt{\frac{a}{aL_{<} + aL_{>} + 2L_{<}L_{>}}} \quad (\text{A} \cdot 10)$$

$$L_{\text{RGO}_0} = L_1 + L_2 = L_{<} + L_{>} \quad (\text{A} \cdot 11)$$

$$L_1 = \rho_0 - a = \text{QQ}_0, \quad L_2 = \rho - a = \text{Q}_0\text{P}. \quad (\text{A} \cdot 12)$$

The notation \hat{A}_{j,RGO_0} denotes a divergence factor of RGO_0 [2], [3], and $L_{<}$ ($L_{>}$) is a symbol for the smaller (larger) in L_1 and L_2 . In (A·9), $R_{j,11}$ is a reflection coefficient on the *convex side* at the point Q_0 on the coating surface (see Fig. 2) and is defined by

$$R_{j,11} = \begin{cases} -\frac{\sqrt{\varepsilon_{2r}} - \sqrt{\varepsilon_{1r}}}{\sqrt{\varepsilon_{2r}} + \sqrt{\varepsilon_{1r}}} & \text{for } j = \text{E} \\ +\frac{\sqrt{\varepsilon_{2r}} - \sqrt{\varepsilon_{1r}}}{\sqrt{\varepsilon_{2r}} + \sqrt{\varepsilon_{1r}}} & \text{for } j = \text{H} \end{cases}. \quad (\text{A} \cdot 13)$$

A.3 Symbols A_{j,RGO_p} and L_{RGO_p} of RGO_p , $p = 1, 2, \dots, M_j$ in (A·2)

The symbols A_{j,RGO_p} and L_{RGO_p} of RGO_p , $p = 1, 2, \dots, M_j$ propagating along the path $Q \rightarrow p(Q_0 \rightarrow R \rightarrow)Q_0 \rightarrow P$, which is emitted at the point Q and then reflected p times at the point R including the multiple reflection effect $p(Q_0 \rightarrow R \rightarrow)Q_0$ before arriving at the point P (see Fig. 2), are given by [23]

$$A_{j,\text{RGO}_p} = \hat{A}_{j,\text{RGO}_p} T_{j,12} (R_{j,2})^p (R_{j,22})^{p-1} T_{j,21} \quad (\text{A} \cdot 14)$$

$$\hat{A}_{j,\text{RGO}_p} = \sqrt{\frac{a}{aL_{<} + aL_{>} + 2L_{<}L_{>} + D_p}} \quad (\text{A} \cdot 15)$$

$$D_p = \frac{p(a + L_{<})(a + L_{>})(2h)}{a - h} \sqrt{\frac{\varepsilon_{1r}}{\varepsilon_{2r}}} \quad (\text{A} \cdot 16)$$

$$L_{\text{RGO}_p} = L_{<} + p\sqrt{\frac{\varepsilon_{2r}}{\varepsilon_{1r}}}(2h) + L_{>}. \quad (\text{A} \cdot 17)$$

The notation \hat{A}_{j,RGO_p} is a divergence factor of RGO_p . In (A·14), $T_{j,12}$ ($T_{j,21}$) denotes a transmission coefficient from medium 1 (medium 2) to medium 2 (medium 1) at the point Q_0 (see Fig. 2) and is given by

$$T_{j,12} = \begin{cases} \frac{2\sqrt{\varepsilon_{1r}}}{\sqrt{\varepsilon_{2r}} + \sqrt{\varepsilon_{1r}}} & \text{for } j = \text{E} \\ \frac{2\sqrt{\varepsilon_{2r}}}{\sqrt{\varepsilon_{2r}} + \sqrt{\varepsilon_{1r}}} & \text{for } j = \text{H} \end{cases} \quad (\text{A} \cdot 18)$$

$$T_{j,21} = \begin{cases} \frac{2\sqrt{\varepsilon_{2r}}}{\sqrt{\varepsilon_{2r}} + \sqrt{\varepsilon_{1r}}} & \text{for } j = \text{E} \\ \frac{2\sqrt{\varepsilon_{1r}}}{\sqrt{\varepsilon_{2r}} + \sqrt{\varepsilon_{1r}}} & \text{for } j = \text{H} \end{cases}. \quad (\text{A} \cdot 19)$$

The notations $R_{j,2}$ and $R_{j,22}$ denote a reflection coefficient at the point R and that on the *concave side* at the point Q_0 on the coating surface (see Fig. 2) and are defined by

$$R_{j,2} = \begin{cases} -1 & \text{for } j = \text{E} \\ +1 & \text{for } j = \text{H} \end{cases} \quad (\text{A} \cdot 20)$$

$$R_{j,22} = \begin{cases} +\frac{\sqrt{\varepsilon_{2r}} - \sqrt{\varepsilon_{1r}}}{\sqrt{\varepsilon_{2r}} + \sqrt{\varepsilon_{1r}}} & \text{for } j = \text{E} \\ -\frac{\sqrt{\varepsilon_{2r}} - \sqrt{\varepsilon_{1r}}}{\sqrt{\varepsilon_{2r}} + \sqrt{\varepsilon_{1r}}} & \text{for } j = \text{H} \end{cases}. \quad (\text{A} \cdot 21)$$

The HF asymptotic solution for a backward transient scattering field component in (A·2), which constitutes the TD-SPT in (A·1), satisfies the reciprocity principle [30], since the same solution is obtained when the locations of a source point Q and an observation point P are swapped.



Keiji Goto received the B.E. and M.E. degrees (equivalents) from the National Defense Academy of Japan, Yokosuka, Japan, in 1984 and 1989, respectively, and the D.E. degree from the University of Tsukuba, Tsukuba, Japan, in 2001. From 1991 to 1996, he was a Researcher at the National Defense Academy of Japan. From 1996 to 2004, he was worked as a Researcher at the Japan Ground Self-Defense Force and at the Defense Agency (now the Ministry of Defense) in Japan. Since March 2004, he has been with

the National Defense Academy of Japan, where he is currently a Professor. His current research interests include high-frequency scattering in the frequency and time domains. Dr. Goto received the Paper Presentation Award from the Institute of Electrical Engineers of Japan in 1993.



Toru Kawano received the B.E., M.E., and D.E. degrees in electrical engineering from Hosei University, Tokyo, Japan, in 1995, 1997, and 2001, respectively. Since April 2001, he has been with the National Defense Academy of Japan, where he is currently an Associate Professor. His current research interests include the scattering and propagation of electromagnetic waves, and antennas. Dr. Kawano received the Paper Presentation Award from the Institute of Electrical Engineers of Japan in 2008.

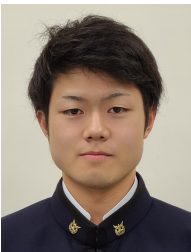


Munetoshi Iwakiri received the B.E. degree in Computer Science in 1993 and the M.E. degree in Mathematics and Computer Science in 1998 from the National Defense Academy of Japan, Yokosuka, Japan. In 1999, he joined the Department of Computer Science, the National Defense Academy of Japan, as a Research Associate. In 2002, he received the D.E. degree from Keio University, Tokyo, Japan. In 2005, he became a Lecturer and in 2015, he became an Associate Professor in the same institution. His

research interests include multimedia processing and information security.



Tsubasa Kawakami is currently a member of the undergraduate course of the Department of Communications Engineering at the National Defense Academy of Japan, Yokosuka, Japan. Her current research interests include high-frequency scattering of electromagnetic waves.



Kazuki Nakazawa is currently a member of the undergraduate course of the Department of Communications Engineering at the National Defense Academy of Japan, Yokosuka, Japan. His current research interests include high-frequency scattering of electromagnetic waves.

PAPER

10-Gbit/s Data Transmission Using 120-GHz-Band Contactless Communication with SRR Integrated Glass Substrate

Tomohiro KUMAKI[†], *Student Member*, Akihiko HIRATA^{†a)}, *Senior Member*, Tubasa SAIJO^{††}, *Nonmember*, Yuma KAWAMOTO^{††}, *Student Member*, Tadao NAGATSUMA^{††}, *Fellow*, and Osamu KAGAYA^{†††}, *Member*

SUMMARY We achieved 10-Gbit/s data transmission using a cutting-edge 120-GHz-band high-speed contactless communication technology, which allows seamless connection to a local area network (LAN) by simply placing devices on a desk. We propose a glass substrate-integrated rectangular waveguide that can control the permeability of the top surface to 120-GHz signals by contacting a dielectric substrate with the substrate. The top surface of the rectangular waveguide was replaced with a glass substrate on which split-ring resonators (SRRs) were integrated. The transmission loss of the waveguide with a glass substrate was 2.5 dB at 125 GHz. When a dielectric sheet with a line pattern formed on the contact surface was in contact with a glass substrate, the transmission loss from the waveguide to the dielectric sheet was 19.2 dB at 125 GHz. We achieved 10-Gbit/s data transmission by contacting a dielectric sheet to the SRR-integrated glass substrate.

key words: millimeter-wave wireless communications, bandstop filter, bandpass filter, metasurface

1. Introduction

The use of wireless local area networks (LAN) is expanding because they do not require wired cable connections and allow mobile terminals to freely connect to networks at various locations in a room. With increasing demands, wireless LANs are becoming increasingly faster, with transmission speeds of up to 6.9 Gbit/s for IEEE 802.11.ac [1] and 9.6 Gbit/s for IEEE 802.11.ax [2]. However, conventional wireless LAN technology limits the number of channels of access points and interchannel interference, resulting in unstable communication [3].

Sheet LAN is a potential candidate for addressing wireless LAN issues, including access concentration and interference at access points [4]. It is a new communication method that enables contactless connection with a LAN by simply placing mobile devices on a desk. A desk mounted with a LAN sheet is already in use. Sheet LAN transmits radio waves in the 5-GHz band by confining radio waves inside a dielectric sheet, achieving a maximum transmission speed of 300 Mbit/s [5]. One way to increase the data rate of the sheet LAN is to use a > 100-GHz-band millimeter-wave (MMW)

signal. Data transmissions of 10 Gbit/s and > 100 Gbit/s have been reported using 120 and 300 GHz wireless links, respectively [6]–[12].

In order to investigate how to boost the data rate of sheet LAN by utilizing a 120-GHz-band signal, we have been developing a 120-GHz-band sheet LAN technology [4]. In this study, a 120-GHz-band signal was transmitted in a dielectric sheet (Rogers RT/duroid 5880 [13]), and we achieved 10-Gbit/s data transmission. However, due to the MMW signal's high transmission loss [14], creating a 120-GHz band sheet LAN with a length of more than 1 m is challenging. For achieving a transmission distances of several meters, we investigate sheet LAN with hollow rectangular waveguides characterized by a low transmission loss of > 100-GHz-band signals. However, even if the receiver is in contact with the hollow rectangular waveguide, it cannot pick up radio signals traveling through it because the metal plates surrounding the waveguide's propagation route prevent it from doing so. We have proposed a hollow rectangular waveguide with split ring resonator (SRR)-integrated glass substrates in place of a metal plate on the top surface of the waveguide in order to achieve > 10-Gbps data transmission in a sheet LAN [15]. An SRR can produce the desired magnetic susceptibility (magnetic response), creating the necessary strong magnetic coupling with an applied electromagnetic field [16]–[20]. We developed 120-GHz-band radio wave absorbers and bandpass filters based on SRRs and successfully achieved 10 Gbit/s data transmission over 120-GHz-band wireless links using these devices [21]–[25]. The SRR integrated on the surface of the glass substrate reflected a 120-GHz-band signal traveling in the hollow waveguide, and the measured transmission loss of the glass-integrated rectangular waveguide was approximately 5 dB at 125 GHz. A portion of the millimeter-wave signal flowing in the waveguide was routed through the glass substrate to the dielectric sheet when a dielectric sheet was placed on the glass substrate. The transmission loss from the waveguide to the dielectric sheet was 21.2 dB at 125 GHz.

This paper presents a 10-Gbit/s data transmission with a 120-GHz-band close-proximity wireless link that employs a hollow rectangular waveguide with an SRR-integrated glass substrate. The transmission characteristics of a hollow rectangular waveguide with an SRR-integrated glass substrate were improved by increasing the precision of the mounting position on the glass substrate. Next, the transmission loss from the waveguide to the dielectric sheet in contact with

Manuscript received June 15, 2023.

Manuscript revised November 10, 2023.

Manuscript publicized February 8, 2024.

[†]Dept. of Information and Communication Systems Engineering, Chiba Institute of Technology, Narashino-shi, 275–0016 Japan.

^{††}Osaka University, Toyonaka-shi, 560–0043 Japan.

^{†††}Materials Integration Laboratories, AGC Inc., Yokohama-shi, 230–0045 Japan.

a) E-mail: hirata.akihiko@p.chibakoudai.jp

DOI: 10.1587/transele.2023ECP5024

the glass substrate was reduced by integrating line patterns on the contact surface of the dielectric sheet. We conducted a data transmission experiment using a hollow rectangular waveguide with an SRR-integrated glass substrate and a dielectric sheet with line patterns and succeeded in 10-Gbit/s data transmission.

2. Design of Hollow Rectangular Waveguide with Split Ring Resonator Integrated Glass Substrate

Figure 1 shows a conceptual diagram of the proposed sheet LAN system. A portion of the top surface of the hollow waveguide was removed, and a glass substrate was placed on the top surface to form the surface. The SRRs on the glass substrate reflect the 120-GHz-band MMW signal traveling in the hollow rectangular waveguide when no dielectric sheet is in contact with the glass substrate, as shown in Fig. 1 (a), which reduces the transmission loss from Port 1 to Port 2. When a dielectric sheet with line patterns is in contact with a glass substrate (Fig. 1 (b)), the resonant characteristics of the SRRs change, and a portion of the millimeter-wave signal propagating in the waveguide is guided through the glass substrate to the dielectric sheet.

Figure 2 shows schematics of the simulation models for full 3D electromagnetic (EM) simulations based on the finite element method (ANSYS HFSS). The size of the glass substrate was 7.714 mm × 3.6 mm, and the thickness of the glass substrate was 0.2 mm. The SRRs on the glass substrate were formed by a 5-μm-thick gold film. The manufacturing process was carried out according to the following procedures. First, Ti/Pd thin film was formed on the quartz substrate. After resist coating and resist pattern formation, SRR patterns are formed by gold plating. Next, after stripping the resist, the unnecessary Ti/Pd thin film is removed by etching. The gold conductivity was set to 41000000 siemens/m. The size of the hollow rectangular waveguide was 2 mm × 1 mm, and its length was 12.7 mm. Rogers RT/Duroid 5880 was used as a dielectric sheet. The width and thickness of the di-

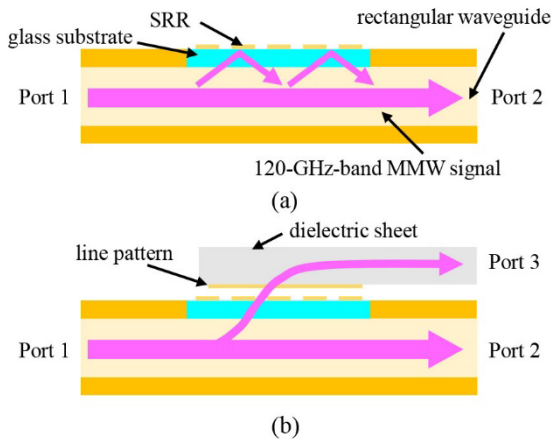


Fig. 1 Concept diagram of the LAN sheet system (a) when no dielectric sheet contacts the glass substrate, and (b) when a dielectric sheet contacts with the glass sheet.

electric sheet were 2.5 mm and 0.78 mm, respectively. Two cross-sections of the hollow rectangular waveguide were set up as ports 1 and 2. The section of the dielectric sheet on the same side as Port 2 was designated as port 3. Figure 3 (a) shows the SRR unit cell simulation model. We simulated the transmission loss of the hollow rectangular waveguide with an SRR-integrated glass substrate (S_{21}) for the case where no dielectric sheet is in contact with the dielectric sheet. SRR size parameters are as follows, unit cell size (a): 500 μm, SRR side length (b): 457 μm, capacitor length (c): 200 μm, capacitor gap (d): 21 μm, linewidth (e, L, w1): 87 μm, and gap between impedance and capacitor section (w2): 56 μm.

The dielectric sheet simulation model with added line patterns is shown in Fig. 4. This line pattern is designed to minimize the transmission loss from the rectangular waveguide to the dielectric sheet at 125 GHz when the dielectric sheet contacts the SRR integrated glass substrate. The distance from the edge of the dielectric sheet to the line patterns (f): 152 μm, the line width of the line patterns (g): 120 μm, the distance between the line patterns (h): 155 μm, and line pattern length: 7.5 mm.

Figure 5 shows the simulation results for the hollow waveguide models shown in Fig. 2. We simulated the S_{21}

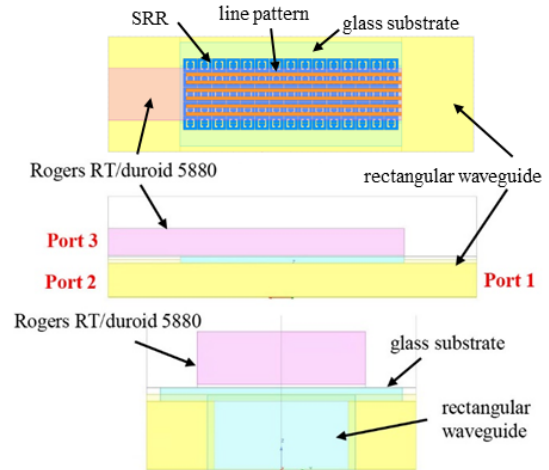


Fig. 2 Schematic diagrams of simulation models for the hollow rectangular waveguide with SRR integrated glass substrate.

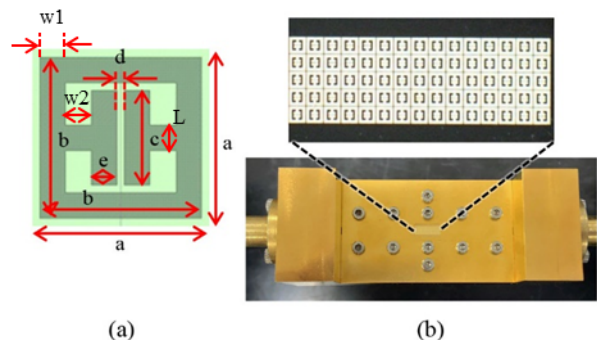


Fig. 3 (a) Schematic diagrams of SRR unit cell, (b) Photograph of SRR integrated glass substrate and waveguide module.

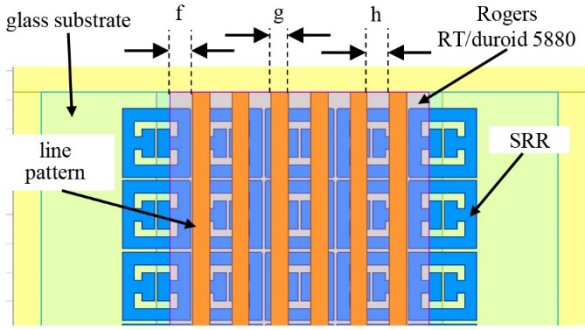


Fig. 4 Schematic diagram of simulation model of dielectric sheet with line pattern added.

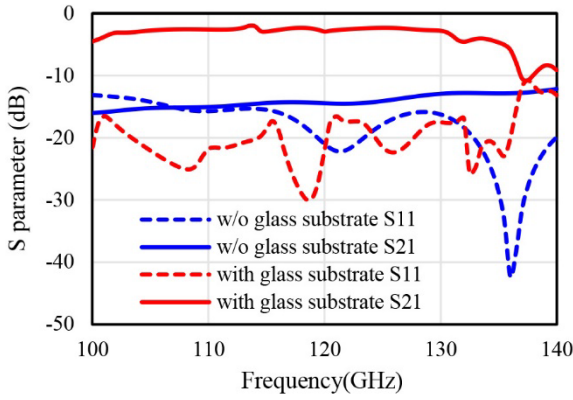


Fig. 5 Simulated S_{21} of the waveguide with SRR integrated glass substrate and without SRR integrated glass substrate.

characteristics of a hollow waveguide with and without a glass substrate on the top surface to investigate the impact of the glass substrate on the transmission properties of the hollow waveguide. S_{21} at 125 GHz was -2.31 dB when the glass substrate was integrated into the hole at the top surface of the hollow waveguide and -14.1 dB when the glass substrate was removed from the hole at the top surface of the hollow waveguide. Figure 6 (a) and 6 (b) show the simulated electric field distributions of the hollow waveguide with and without the glass substrate, respectively. In the electric field distribution of the model without the glass substrate in Fig. 6 (a), the 120-GHz-band signal leaks through the hole at the top surface of the waveguide. When the glass substrate is integrated into the hole at the top surface of the waveguide (Fig. 6 (b)), the 120-GHz-band signal leaking through the hole at the top surface of the waveguide is suppressed, and the transmission loss of the 120-GHz-band signal traveling inside the waveguide is also reduced. Based on these results, the integration of the glass substrate into the hole on the top surface of the waveguide reduces the transmission loss by approximately 11.79 dB.

We prototyped an SRR-integrated glass substrate and waveguide module with a hole of the same size as that of the glass substrate on the top surface of a hollow square waveguide. A glass substrate was attached to the holes. Figure 3 (b) shows a photograph of the prototype SRR-integrated

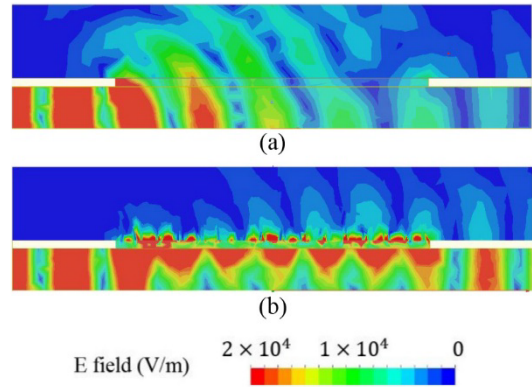


Fig. 6 (a) Simulation results of the electric field distribution without SRR integrated glass substrate. (b) Results of electric field distribution with an SRR integrated glass substrate.

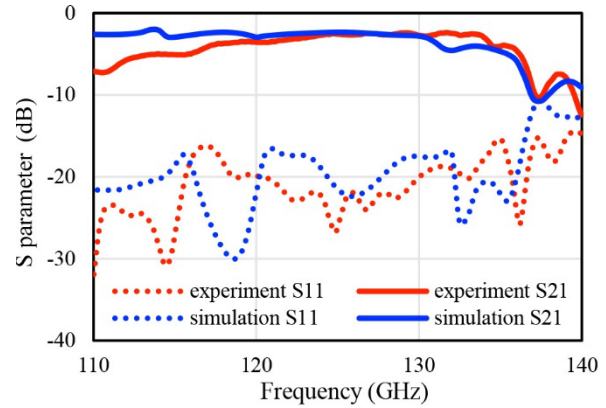


Fig. 7 Measured and simulated S_{11} and S_{21} of the waveguide with SRR integrated glass substrate.

glass substrate and the waveguide module on which the glass substrate was integrated. We measured the transmission loss of the waveguide module using a vector network analyzer (VNA). The frequency extenders of the VNA were connected to both waveguide ports of the waveguide module. Furthermore, we fabricated a waveguide module of the same size with no holes on top and measured its transmission loss. We calculated the difference in the transmission loss between these two modules and defined it as the transmission loss of the waveguide with the SRR-integrated glass substrate.

Figure 7 shows the simulated and measured transmission losses of the waveguide shown in Fig. 3 (a). The simulation results indicated that the transmission loss ranged from 2 to 5 dB at 110-130 GHz. The simulated S_{21} was -2.3 dB at 125 GHz. The measured S_{21} was -2.5 dB at 125 GHz, which is almost the same as the simulated S_{21} . The fluctuation of S_{21} from 115 to 135 GHz was 2.5 dB, and this frequency characteristic was sufficient for 10-Gbit/s data transmission with the ASK modulation scheme. In addition, the transmission losses were higher than those simulated results at 110-120 GHz. We believe that this difference arises from a gap or misalignment of the position of the SRR-integrated glass substrate during mounting.

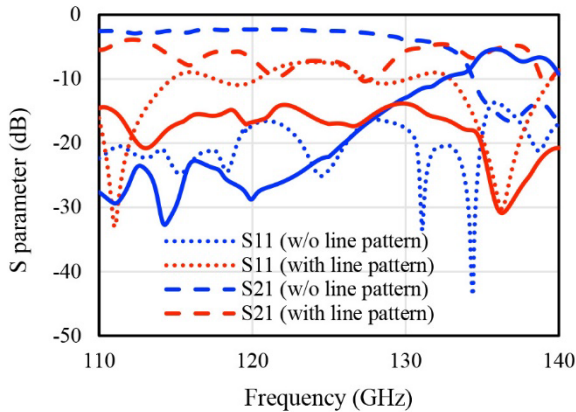


Fig. 8 Simulation results of S parameters with and without line patterns on the dielectric sheet in contact with the top of the waveguide.

3. Contactless Communication Using Dielectric Sheet

We investigated the possibility of extracting part of the millimeter-wave signal propagating in a hollow square waveguide and communicating with it by bringing the dielectric sheet into contact with a glass substrate placed on the top surface of the hollow square waveguide, as shown in Fig. 1 (b). Line pattern was added to the surface of the dielectric sheet in contact with the glass substrate to increase the proportion of 120-GHz-band signal that are guided to the dielectric sheet. Figures 8 and 9 shows the simulation results of S parameters and electric field distribution with and without the line pattern on the dielectric sheet, respectively. The simulation results showed that S_{21} was -2.52 dB and S_{31} was -22.12 dB at 125 GHz, when no line pattern was added to the dielectric sheet, and S_{21} was -7.25 dB and S_{31} was -16.99 dB at 125 GHz when a line pattern was added. The transmission loss tended to be lower at from 110 to 130 GHz when a line pattern was added. In addition, the electric field distribution in Fig. 9 shows that the magnitude of the signal guided to the dielectric sheet is stronger when the line pattern is added (Fig. 9 (c)) compared to that when no line pattern is added (Fig. 9 (a)) at 125 GHz. On the contrary, S_{31} with line pattern is lower than that without line pattern at over 130 GHz. We added the simulation results of electric field distribution at 125 GHz and 135 GHz as Fig. 9. When a dielectric sheet with no line pattern is in contact at 135 GHz (Fig. 9 (b)), a standing wave is generated at the glass substrate and the waveguide below it, and the 135 GHz band signal does not travel in the waveguide beyond the glass substrate. As a result, the leaked 135 GHz band signal is considered to have been guided to the dielectric sheet. On the other hand, the obvious standing wave was not observed at 135 GHz in case of the dielectric sheet without line pattern (Fig. 9 (d)). The presence or absence of these standing waves may be the cause of the difference in S_{31} at over 130 GHz. These results indicate that adding a line pattern to the dielectric sheet can guide 125 GHz signals to the dielectric sheet side.

Then, the transmission loss from the waveguide to the

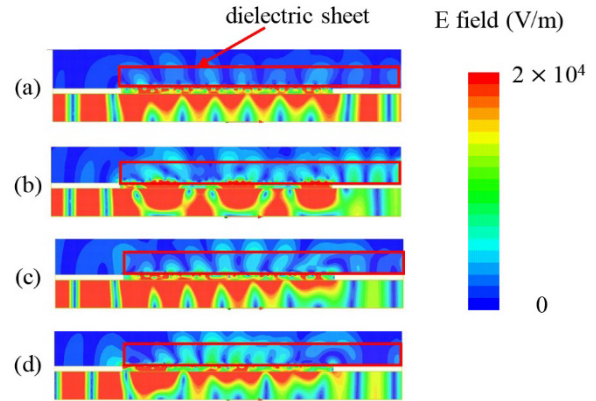


Fig. 9 (a, b) Simulation results of electric field distribution at 125 GHz (a) and 135 GHz (b) when line patterns are not formed on dielectric sheets. (c, d) Simulation results of the electric field distribution at 125 GHz (c) and 135 GHz (d) when the line patterns are formed on the dielectric sheet.

dielectric sheet was measured using a VNA. Figure 10 (a) shows a photograph of the measurement setup. A frequency extender was attached to the waveguide port of the waveguide module (Port 1), and another frequency extender was attached to the dielectric sheet (Port 3). The other waveguide port (Port 2) was terminated using a waveguide load. Rogers RT/Duroid 5880 was used as the dielectric sheet. The length, width, and thickness of the dielectric sheets were 100, 2.5, and 0.78 mm, respectively. One of the dielectric sheet's tips was tapered, and the tapered section was inserted into the frequency extender's waveguide to reduce transmission loss at Port 3. The other tip of the dielectric sheet is attached to the glass substrate. Figure 10 (b) shows a photograph of the tip of the dielectric sheet in contact with the glass substrate. A 100 mm-long dielectric sheet was connected to the waveguide port of the frequency extender by bending it such that it did not hit the waveguide module.

Figure 11 shows the measurement results of the transmission loss from the waveguide to the dielectric sheet in contact with and without the glass substrate on the hollow rectangular waveguide. The measured S_{31} at 125 GHz was -18.8 dB in case the line patterns are formed on the dielectric sheet, that was -23.7 dB in case there is no line pattern on the dielectric sheet. Therefore, the use of line pattern on the dielectric sheet decreases the transmission loss from the waveguide to the dielectric sheet by 4.9 dB.

It is important to evaluate the effect of bending the dielectric sheet on the transmission properties, because radiation loss occurs at the bending point of the dielectric sheet. Therefore, we measured the increase in the transmission loss of the dielectric sheet when it was bent. When the dielectric sheet was bent twice at 45 degree as shown in the photo in Fig. 10 (a), the increase in transmission loss of the dielectric sheet was approximately 3.5 dB at 125 GHz. The measured S_{31} at 125 GHz was -18.8 dB in case of the dielectric sheet with line pattern. Excluding the effect of bending of the dielectric sheet, the proportion of the 125 GHz signal guided into the dielectric sheet by contact is estimated to be

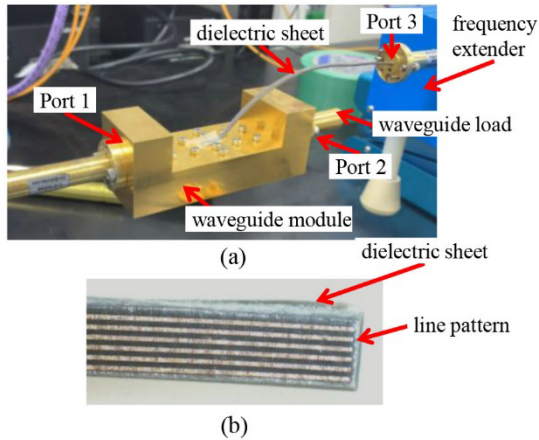


Fig. 10 (a) Photograph of the measurement setup for the transmission loss from the waveguide to the dielectric sheet. (b) Photograph of the tip of the dielectric sheet in contact with the glass substrate.

-15.3 dB. The fluctuation of S_{31} from 118 to 132 GHz was about 3.2 dB. These frequency characteristics are sufficient for 10-Gbit/s data transmission with the ASK modulation scheme.

The measurement results for S_{21} with and without the dielectric sheet in contact, are also shown in Fig. 11. The measurement results showed that S_{21} was -2.6 dB at 125 GHz when the dielectric sheet was not in contact with the glass substrate. On the other hand, measured S_{21} was -4.0 dB and S_{31} was -23.7 dB at 125 GHz, when no line pattern was formed to the dielectric sheet, and S_{21} was -5.1 dB and S_{31} was -17.7 dB at 125 GHz when a line pattern was formed. The measured transmission loss of a hollow rectangular waveguide with SRR integrated glass substrate increased by 1.4 dB when the dielectric sheet without line patterns was in contact with the glass substrate. This is because a portion of the MMW signal propagating in the hollow rectangular waveguide is guided by the dielectric sheet. On the other hand, the simulation results in Fig. 7 and 8 shows that the transmission loss increased by 0.2 dB by contacting the dielectric sheet without line pattern. We suppose that the difference of the increase in the transmission loss by contacting the dielectric sheet without line pattern between the experiment and the simulation can be attributed to the difference in the actual contact conditions between the glass and the dielectric sheet in the experiment and the simulation model.

The experimental result of S_{21} at is 1.5 dB larger than the simulation result of S_{21} in case the dielectric sheet without line pattern was in contact with the glass substrate. On the other hand, the experimental result of S_{21} is 2.2 dB smaller than the simulation result of S_{21} when the dielectric sheet with line pattern was in contact with the glass substrate. Moreover, the simulation and experimental results deviated significantly at frequencies above 130 GHz. The reason for this is thought to be the difference between the simulation model and the actual waveguide module and the differences in the contact conditions between the dielectric sheet and the

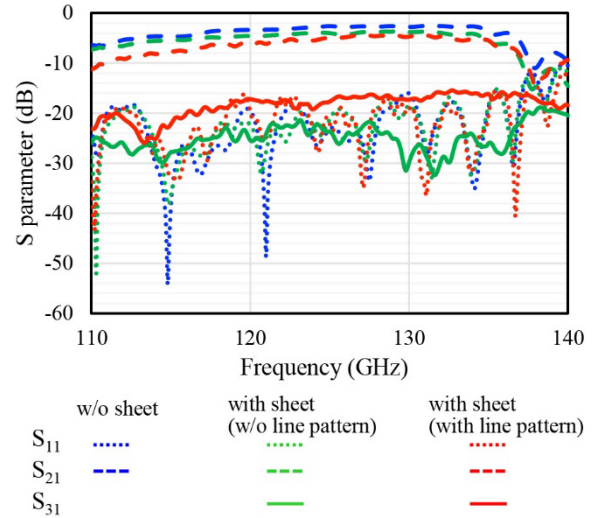


Fig. 11 Measurement results of the transmission loss from the waveguide to the dielectric sheet in contact with and without the glass substrate on the hollow rectangular waveguide.

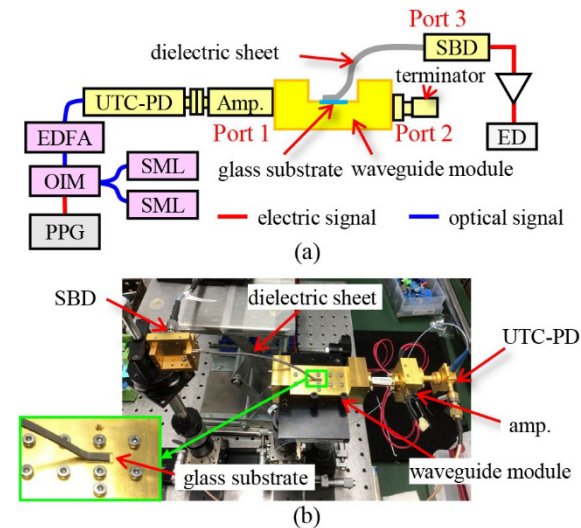


Fig. 12 (a) Schematic diagram and (b) photograph of experimental setup for data transmission characteristics of contactless communication.

glass substrate.

Finally, we verified the feasibility of data transmission through a dielectric sheet by contacting it with a glass-substrate-integrated hollow waveguide. Figures 12 (a) and 12 (b) show a schematic diagram and photograph of the experimental setup for data transmission characteristics of contactless communication using the dielectric sheet and hollow rectangular waveguide with an SRR-integrated glass substrate, respectively. The measurement setup for data transmission employed an ASK modulation scheme and envelope detection. The 120-GHz-band transmitter employs the optical generation of 120-GHz-band wireless signals based on two-mode beating. A 125-GHz-band optical subcarrier signal was generated by combining the output of two single-mode lasers (SMLs) and an optical intensity modulator

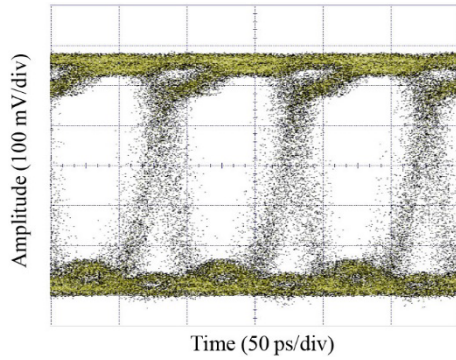


Fig. 13 Bit error rate (BER) characteristics of the wireless data transmission system at a data rate of 10.0 Gbit/s.

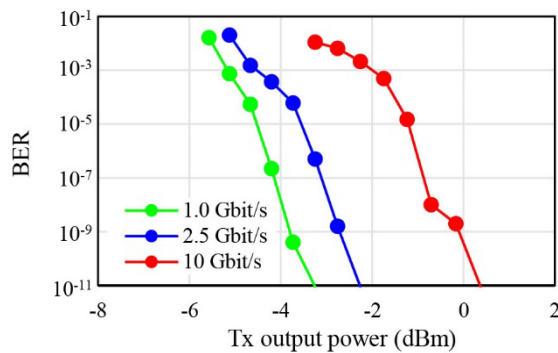


Fig. 14 Bit error rate (BER) characteristics of the wireless data transmission system at a data rate of 10.0 Gbit/s.

(OIM) modulated 125-GHz-band optical subcarrier signal using 10 Gbit/s data generated by a pulse pattern generator (PPG). The optical signal was amplified by an erbium-doped fiber amplifier (EDFA) and input into a uni-traveling carrier photodiode (UTC-PD) module [26]–[28], which converted the optical subcarrier signal to a 120-GHz-band MMW signal. The O/E-converted signal was amplified using a 120-GHz-band amplifier module [29], [30]. The waveguide output port of the amplifier module was connected to Port 1 of the waveguide module, as shown in Fig. 12(a). Port 2 of the waveguide module was terminated using a waveguide terminator. One of the tips of the 100-mm-long dielectric sheet was in contact with the glass substrate of the waveguide module, and the other tip of the dielectric sheet was inserted into the input port of the Schottky barrier diode (SBD) detector. The demodulated data signals are amplified using a baseband amplifier and fed into an error-rate detector (ED) or sampling oscilloscope. Figure 12 shows the eye pattern of the demodulated 10 Gbit/s data signal when the Tx output power was 0.5 dBm. Clear eye opening was observed. Figure 14 shows the dependence of the bit error rate (BER) characteristics of contactless communication on the Tx output power. Tx output power was measured at the output port of the 120-GHz-band amplifier module by connecting a power meter instead of the waveguide module. A bit error rate (BER) of below 10^{-11} was obtained with a transmission power of over -2.5 dBm at a data rate of 2.5 Gbit/s.

When the data rate was 10 Gbit/s, a BER below 10^{-11} was obtained with a Tx output power of 0.4 dBm. The BER characteristics at 10 Gbit/s characteristic is significantly degraded from those at 1.0 Gbit/s and 2.5 Gbit/s. As shown in Fig. 11, the transmission characteristics at the dielectric sheet contact are not flat at 118–132 GHz, which is the occupied bandwidth necessary for 10 Gbps data transmission. This fluctuation of the transmission characteristics causes the distortion of the 120-GHz-band wireless signal, which deteriorates the wireless data transmission characteristics at 10 Gbps. Thus, 10 Gbit/s data transmission through a dielectric sheet was achieved by contacting the dielectric sheet with a glass-substrate-integrated hollow waveguide.

4. Conclusions

We developed a hollow rectangular waveguide with an SRR-integrated glass substrate and applied it to a 120-GHz-band high-speed contactless communication. The SRR integrated on the surface of the glass substrate reflects a 120-GHz-band signal traveling in the hollow waveguide. The transmission loss of the hollow rectangular waveguide with the SRR-integrated glass substrate was 2.5 dB at 125 GHz. The transmission loss from waveguide to dielectric sheet at 125 GHz was 19.2 dB when the dielectric sheet was in contact with a glass substrate and had a line pattern established on the contact surface. We succeeded in 10-Gbit/s data transmission through a dielectric sheet by contacting the dielectric sheet with a glass-substrate-integrated hollow waveguide. These technologies enable high-speed contactless connections with LAN by simply placing mobile devices on a desk.

Acknowledgments

This study was partially supported by MEXT KAKENHI (grant number: JP 21H01328).

References

- [1] W.-S. Jung and Y.-B. Ko, "IEEE 802.11 ac based client centered indoor positioning system," 2016 IEEE Canadian Conference on Electrical and Computer Engineering (CCECE), Vancouver, BC, Canada, pp.1–4, 2016.
- [2] M.M. Hasan and M. Arifuzzaman, "VAQ-EDCA: Additional Video Access Queue Based EDCA Technique for Dense IEEE 802.11 AX Networks," 2019 International Conference on Computer, Communication, Chemical, Materials and Electronic Engineering (IC4ME2), pp.1–4, 2019.
- [3] J. Oh and Y.J. Chong, "Interference alignment for frequency selective fading channels in wireless local area network," 2017 Int. Conf. on Information and Communication Technology Convergence (ICTC), Jeju, Korea (South), pp.999–1001, 2017.
- [4] M. Ushio, F. Tokoro, A. Hirata, T. Higashimoto, Y. Uemura, T. Nagatsuma, N. Sekine, I. Watanabe, and A. Kasamatsu, "10-Gbit/s Data Transmission over Dielectric Sheet for 120-GHz-band Sheet LAN," 2020 International Symposium on Antennas and Propagation (ISAP), Osaka, Japan, pp.543–544, 2021.
- [5] <https://www.itoki-global.com/discover/history/>
- [6] A. Hirata, M. Harada, and T. Nagatsuma, "120-GHz wireless link using photonic techniques for generation, modulation, and emission

- of millimeter-wave signals,” *IEEE Journal of Lightwave Technology*, vol.21, no.10, pp.2145–2153, Oct. 2003.
- [7] A. Hirata, T. Kosugi, H. Takahashi, J. Takeuchi, H. Togo, M. Yaita, N. Kukutsu, K. Aihara, K. Murata, Y. Sato, T. Nagatsuma, and Y. Kado, “120-GHz-band wireless link technologies for outdoor 10-Gbit/s data transmission,” *IEEE Trans. Microw. Theory Tech*, vol.60, no.3, pp.881–895, March 2012.
 - [8] A. Dogadaev, A.V. Lavrinenko, and I.T. Monroy, “Capacity analysis for high-speed terahertz wireless communications,” *Int. Conf. Infrared, Millimeter, and Terahertz Waves*, 2012.
 - [9] J. Takeuchi, A. Hirata, H. Takahashi, N. Kukutsu, Y. Yamada, K. Kitamura, and M. Teshima, “10-Gbit/s bidirectional and 20-Gbit/s unidirectional 2-ch wireless data transmission system using 120-GHz-band finline orthomode transducers,” *IEICE Trans. Electron.*, vol.E97-C, no.2, pp.101–110, Feb. 2014.
 - [10] S. Koenig, D. Lopez-Diaz, J. Antes, F. Boes, R. Henneberger, A. Leuther, A. Tessmann, R. Schmogrow, D. Hillerkuss, R. Palmer, T. Zwick, C. Koos, W. Freude, O. Ambacher, J. Leuthold, and I. Kallfass, “Wireless sub-THz communication system with high data rate,” *Nat. Photonics*, vol.7, no.12, pp.977–981, 2013.
 - [11] H. Takahashi, A. Hirata, J. Takeuchi, N. Kukutsu, T. Kosugi, and K. Murata, “120-GHz-band 20-Gbit/s transmitter and receiver MMICs using quadrature phase shift keying,” 2012 7th European Microwave Integrated Circuit Conference, pp.313–316, 2012.
 - [12] H. Hamada, H. Nosaka, T. Tsutsumi, H. Sugiyama, H. Matsuzaki, H.-J. Song, G. Itami, T. Fujimura, I. Abdo, and K. Okada, “Millimeter-wave InP device technologies for ultra-high speed wireless communications toward beyond 5G,” 2019 IEEE International Electron Devices Meeting (IEDM), pp.9.2.1–9.2.4, 2019.
 - [13] <https://www.rogerscorp.com/advanced-electronics-solutions/rt-duroid-laminates/rt-duroid-5880-laminates>
 - [14] F. Parment, A. Ghiotto, T.-P. Vuong, J.-M. Duchamp and K. Wu, “Broadband transition from dielectric-filled to air-filled Substrate Integrated Waveguide for low loss and high power handling millimeter-wave Substrate Integrated Circuits,” 2014 IEEE MTT-S International Microwave Symposium (IMS2014), Tampa, FL, USA, pp.1–3, 2014.
 - [15] T. Kumaki, S. Ozeki, A. Hirata, and O. Kagaya, “120-GHz-band Close-Proximity Wireless Communication Using Metamaterial Integrated Glass Substrate,” 2022 IEEE International Workshop on Electromagnetics: Applications and Student Innovation Competition (iWEM), Narashino, Japan, 2022, pp.87–88, 2022.
 - [16] D. Kitayama, H.-J. Song, and M. Yaita, “Investigation of plasmon hybridization in split-ring resonators,” 2014 Asia-Pacific Microwave Conference, TH1G-32, 2014.
 - [17] X. Cheng, D.E. Senior, J.J. Whalen, and Y.-K. Yoon, “Electrically small tunable split ring resonator antenna,” 2010 IEEE Antennas and Propagation Society Int. Symp., pp.41–44, 2010.
 - [18] H. Tao, C.M. Bingham, A.C. Strikwerda, D. Pilon, D. Shrekenhamer, N.I. Landy, K. Fan, X. Zhang, W.J. Padilla, and R.D. Averitt, “Highly flexible wide angle of incidence terahertz metamaterial absorber: Design, fabrication, and characterization,” *Physical Review B*, vol.78, no.24, 2008.
 - [19] E.R. Afthar, M.R. Hidayat, and A. Munir, “Analysis of Equivalent Circuit for Bandpass Filter,” The 22nd Asia-Pacific Conference on Communications, pp.361–364, 2016.
 - [20] M.K.T. Al-Nuaimi and W.G. Whittow, “Compact Microstrip Band Stop Filter Using SRR and CSSR: Design, Simulation and Results,” European Conference on Antennas and Propagation, pp.2–6, 2010.
 - [21] A. Hirata and J. Hirokawa, “Absorber integrated planar slot array antenna for suppression of multiple reflection in 120-GHz-band close-proximity wireless system,” *IEICE Trans. Electron.*, vol.E101-C, no.10, pp.791–800, Oct. 2018.
 - [22] K. Itakura, A. Hirata, M. Sonoda, T. Higashimoto, T. Nagatsuma, T. Tomura, J. Hirokawa, N. Sekine, I. Watanabe, and A. Kasamatsu, “Control of 120-GHz-band split ring resonator filter by coupling lattice pattern substrate,” *IEICE Trans. Electron.*, vol.E104-C, no.3, pp.102–111, March 2020.
 - [23] A. Hirata, K. Itakura, T. Higashimoto, Y. Uemura, T. Nagatsuma, T. Tomura, J. Hirokawa, N. Sekine, I. Watanabe, and A. Kasamatsu, “Transmission characteristics control of 120 GHz-band bandstop filter by coupling alignment-free lattice pattern,” *IEICE Trans. Electron.*, vol.E104-C, no.10, pp.587–595, Oct. 2021.
 - [24] A. Hirata, T. Saijo, Y. Kawamoto, T. Nagatsuma, I. Watanabe, N. Sekine, and A. Kasamatsu, “Evaluation of transmission characteristics of 120-GHz-band close-proximity wireless links using splitting-resonator absorber integrated planar slot antenna,” *IEICE Trans. Electron.*, vol.E106.C, no.9, pp.458–465, 2023.
 - [25] K. Itakura, A. Hirata, T. Higashimoto, Y. Uemura, T. Nagatsuma, I. Watanabe, N. Sekine, A. Kasamatsu, “Pass Bandwidth Extension of 120-GHz-Band SRR Filter by Coupling Lattice Pattern Substrate,” International Topical Meeting on Microwave Photonics, Th-P27, Nov. 2020.
 - [26] T. Ishibashi, T. Furuta, H. Fushimi, S. Kodama, H. Ito, T. Nagatsuma, N. Shimizu, and Y. Miyamoto, “InP/InGaAs uni-traveling-carrier photodiodes,” *IEICE Trans. Electron.*, vol.E83-C, no.6, pp.938–949, 2000.
 - [27] H. Ito, T. Furuta, S. Kodama, and T. Ishibashi, “InP/InGaAs uni-traveling-carrier photodiode with a 310 GHz bandwidth,” *Electron. Lett.*, vol.36, no.21, pp.1809–1810, 2000.
 - [28] H. Ito, T. Ito, Y. Muramoto, T. Furuta, and T. Ishibashi, “F-band (90–140 GHz) uni-traveling-carrier photodiode module for a photonic local oscillator,” *Int. Symp. on Space Terahertz Technol.*, pp.318–327, 2010.
 - [29] T. Kosugi, M. Tokumitsu, K. Murata, T. Enoki, H. Takahashi, A. Hirata, and T. Nagatsuma, “120-GHz Tx/Rx Waveguide Modules for 10-Gbit/s Wireless Link System,” *IEEE CSIC Symp. Dig.*, pp.25–28, Nov. 2006.
 - [30] A. Hirata, T. Kosugi, H. Takahashi, J. Takeuchi, K. Murata, N. Kukutsu, Y. Kado, S. Okabe, T. Ikeda, F. Suginosita, K. Shogen, H. Nishikawa, A. Irino, T. Nakayama, and N. Sudo, “5.8-km 10-Gbps data transmission over a 120-GHz-band wireless link,” 2010 IEEE International Conference on Wireless Information Technology and Systems (ICWITS), 2010.



Tomohiro Kumaki received his B.S. degrees in engineering in 2022 from Chiba Institute of Technology, Chiba, Japan, where he is currently working toward the M.S. degree with the Graduate School of Engineering. Mr. Kumaki is a student member of IEICE.



Akihiko Hirata received his B.S. and M.S. degrees in chemistry and his Dr. Eng. degree in electrical and electronics engineering from Tokyo University, Tokyo, Japan, in 1992, 1994, and 2007, respectively. He joined the Atsugi Electrical Communications Laboratories of Nippon Telegraph and Telephone Corporation (presently NTT Device Technology Laboratories) in Kanagawa, Japan, in 1994. He was a senior research engineer and supervisor at NTT Device Technology Laboratories. He has been a professor at the

Chiba Institute of Technology since 2016. His current research involves millimeter-wave antennas and ultra-broadband millimeter-wave wireless systems. Prof. Hirata is a senior member of IEEE and a senior member of IEICE.



Tsubasa Saijo received the B.S. degree in engineering science in 2020 from Osaka University, Osaka, Japan, where he is currently working toward the M.S. degree with the Graduate School of Engineering Science. His research focuses on the secure wireless communication by combining terahertz and optical waves.



Yuma Kawamoto received the B.S. degree in engineering science in 2020 from Osaka University, Osaka, Japan, where he is currently working toward the M.S. degree with the Graduate School of Engineering Science. His research focuses on the integration and packaging of THz devices for wireless communications. Mr. Kawamoto is a student member of IEICE.



Tadao Nagatsuma received his B.S., M.S., and Ph.D. degrees in electronic engineering from Kyushu University, Fukuoka, Japan, in 1981, 1983, and 1986, respectively. In 1986, he joined the Electrical Communications Laboratories, Nippon Telegraph and Telephone Corporation (NTT), Atsugi, Kanagawa, Japan. From 1999 to 2002, he was a Distinguished Technical Member with NTT Telecommunications Energy Laboratories. From 2003 to 2007, he was a Group Leader with NTT Microsystem Integra-

tion Laboratories and was an NTT Research Professor from 2007 to 2009. Since 2007, he has been with Osaka University, Osaka, Japan, where he is currently a Professor with the Division of Advanced Electronics and Optical Science, Department of Systems Innovation, Graduate School of Engineering Science. His research interests include ultrafast electronics and millimeter-wave and terahertz photonics. Dr. Nagatsuma is a Fellow of the IEEE, and a Fellow of the Institute of Electronics, Information and Communication Engineers (IEICE), Japan. He currently serves as an Associate Editor of the IEEE Photonics Technology Letters and the IEEE Trans. Terahertz Science and Technology, and a President of the Terahertz Systems Consortium and a Past-Vice President of the IEICE. He was the recipient of numerous awards including the 1989 IEICE Young Engineers Award, the 1992 IEEE Andrew R. Chi Best Paper Award, the 1997 Okochi Memorial Award, the 1998 Japan Microwave Prize, the 2000 Ministers Award of the Science and Technology Agency, the 2002 and 2011 Asia-Pacific Microwave Conference Prize, the 2004 YRP (Yokosuka Research Park) Award, the 2006 Asia-Pacific Microwave Photonics Conference Award, the 2006 European Microwave Conference Prize, the 2007 Achievement Award presented by the IEICE, the 2008 Maejima Award, the 2011 Recognition from Kinki Bureau of Telecommunications, Ministry of Internal Affairs and Communications, the 2011 Commendation for Science and Technology by the Ministry of Education, Culture, Sports, Science and Technology, and the 2014 IEEE Tatsuo Ito Award, and the 2020 Distinguished Achievement and Contributions Award by the IEICE.



Osamu Kagaya received the B.S. and M.E. and D.E. degrees in engineering from the Tokyo University of Agriculture and Technology (TUAT), Tokyo, Japan, in 1999, 2002 and 2022, respectively. He joined AGC Inc. in 2001. Since then, he has been engaged in research on glass antennas and electromagnetic scattering.